Diagrammatic analysis of the density operator for nonlinear optical calculations: Pulsed and cw responses

T. K. Yee and T. K. Gustafson
Department of Electrical Engineering and Computer Sciences and the Electronic Research Laboratory, University of California, Berkeley 94720

(Received 28 February 1977; revised manuscript received 18 November 1977)

In the present paper a diagrammatic analysis of the density operator for the evaluation of nonlinear optical quantities is considered. The present approach extends earlier diagrammatic analysis by treating the time evolution of both the wave function and its complex conjugate. Time-ordered graphs result, each of which corresponds to a term in the density matrix. Examples involving the third-order susceptibility are discussed for both monochromatic and pulse excitation. In particular coherent rotational transient birefringence is discussed. The diagrams provide a convenient means by which nonlinear optical processes can be precisely defined and the susceptibility readily evaluated.

I. INTRODUCTION

In the present paper, we would like to discuss diagrammatic techniques for the evaluation of density-matrix elements to any order of perturbation theory for the purpose of obtaining nonlinear optical susceptibilities and polarizabilities.[1] This approach presents several advantages over a straightforward evaluation of the density-matrix equations. First, since each term of the density matrix for any order of perturbation corresponds to a diagram, a clear and distinct display of the specific perturbation sequence that will result in a particular density-matrix element can be displayed. Thus, the significant density-matrix element contributing to a response can be uniquely and correctly specified. Second, the algebra can be significantly simplified for many calculations, since once rules are established for the evaluation of density-matrix elements associated with a general diagram, perturbation theory is automatically accomplished by applying these rules to specific diagrams. In many cases in nonlinear optical calculations such rules will become more important as the number of density-matrix terms contributing to a nonlinear optical response becomes large. A third significant advantage of the diagrammatic (or Green's-function) approach is that damping is more rigorously included. In contrast to the density-matrix phenomenological damping terms, Green's-function techniques have been utilized to calculate the characteristics of collisional decay from fundamental principles. A fourth advantage to be obtained by the use of diagrams is that many terms calculated from density-matrix perturbation are similar except for time ordering of the various photon interactions. This time ordering, which is clearly displayed diagrammatically, is fundamental and can change the characteristics of otherwise similar nonlinear optical processes.

The diagrammatic evaluation of nonlinear optical susceptibilities has been considered in the past, in particular by Ward,[2] Marcuse,[3] and others. Although many processes could be evaluated by these authors, essential aspects were not included which prevented a full application to the density matrix; in particular, as will be seen, they omitted an account of the time ordering, and a consideration of damping, both of which are crucial. Diagrammatic approaches that have considered the time ordering in nonlinear optical calculations include that of Bonch-Bruevich and Khodovoi,[4] who treated multiphoton absorption probabilities explicitly considering the time ordering. More recently Omont, Smith, and Cooper[5] have utilized such techniques essentially to evaluate the diagonal components of the density matrix (transition rates) to describe resonant spontaneous Raman scattering. The rate of resonant two-quanta absorption, with a consideration of the Doppler profile, using a diagrammatic visualization of the important terms has also recently been presented by Bordé.[6]

In the present paper, we use these diagrammatical techniques for an evaluation of the density-matrix elements and, in particular, for calculations of nonlinear optical polarizations. In order to demonstrate clearly the advantages to be offered by such techniques, we develop the rules for the evaluation of the density-matrix diagram for monochromatic excitation[7] and subsequently apply these techniques to the evaluation of several susceptibilities which have been deduced previously by density-matrix techniques. Following this, the diagrammatic technique is applied to the derivation of transient nonlinear optical responses and, in particular, to that of the molecular rotations excited by electronically resonant ultrashort pulses.

II. GENERAL FORM OF THE DENSITY-MATRIX SOLUTION AND ITS DIAGRAMMATIC REPRESENTATION

The general nth-order perturbational solution to the density matrix has been obtained by several different authors and has been expressed in several different forms. For an arbitrary perturbational Hamiltonian $H'(t)$, the most useful starting point for developing the diagrammatical approach is the expression given by Slichter.[8] Thus the density operator $\rho(t,t)$ can be written

$$\rho(t,t)=\sum_n \rho^{(n)}(t,t), \quad n=0,1,2,\ldots \tag{1}$$

where $\rho^{(n)}(t,t)$ is the nth-order perturbational term and is given by

$$\rho^{(n)}(t,t')=\sum_{lm}\sum_{k=0}^{n}\Big[\int_{-\infty}^{\infty}\cdots\int_{-\infty}^{\infty}\prod_{q=1}^{k}\Big\{K^{+}(t_{q+1},t_q)\frac{H'(t_q)}{i\hbar}\Big\}K^{+}(t_1,t_0)\,|l\rangle\rho_{lm}^{(0)}(t_0)$$
$$\times\langle m|K^{-}(t_0,t_1')\prod_{j=1}^{n-k}\Big\{\frac{H'(t_j')}{-i\hbar}K^{-}(t_j',t_{j+1}')\Big\}$$
$$\times P[U(t-t_k)U(t_k-t_{k-1})\cdots U(t_1-t_{n-k}')U(t_{n-k}'-t_{n-k-1}')$$
$$\times\cdots U(t_1'-t_0)]\,dt_1\cdots dt_1'\cdots\Big]_{\rm av}. \tag{2}$$

In this expression, $K^{+}(t_{q+1},t_q)$ is the retarded Green's function which provides the propagation of the wave function[9] in the absence of an interaction with the field as specified by the perturbation Hamiltonian $H'(t)$. $K^{-}(t_j',t_{j+1}')=[K^{+}(t_{j+1}',t_j')]^{*}$ provides the propagation of the complex-conjugate wave function. $\rho_{lm}^{(0)}(t)$ is the initial value of the lm matrix element of the density operator. In this expression, spatial coordinates have been suppressed since the important features are those associated with temporal evolution. In general, Eq. (2) shows that arbitrary initial values of the density-matrix elements can be taken; however, the usual situations of interest are those for which $l=m$. For the quantum state we shall use the designation $\Phi_n(x)=\Phi_n(r)e^{-i\omega_n t}$ for the wave function, where ω_n is the eigenenergy associated with the unperturbed Hamiltonian H_0. $\Phi_n(r)$ is then the spatial portion of the wave function. This wave function is associated with the state having a ket vector $|n\rangle e^{-i\omega_n t}$. In Eq. (2), $U(t_q-t_{q-1})$ is a unit-step distribution (=1 if $t_q>t_{q-1}$ and 0 if $t_{q-1}>t_q$). These distributions express causality, and a specific ordering of the time variables $t_0,\ldots,t_k$ and of the time variables $t_0,t_1',t_2',\ldots,t_{n-k}'$ associated with the photon interactions to the left and to the right of $\rho_{lm}^{(0)}(t_0,t_0)$, respectively. P specifies that all possible time orderings of the interactions must be taken into account in order to obtain the full solution to $\rho^{(n)}(t,t)$. In practice, only the significant terms arising from all possible time orderings usually are retained. The av in Eq. (2) rigorously introduces damping and linewidth. It is taken over a statistical ensemble of the molecules and, in particular, over variables such as the collisional parameters. The introduction of linewidth and decay in this manner allows one to more easily incorporate collisional theories into nonlinear optics in a rigorous manner.

In Eq. (2) there are three distinct features: those interactions and propagations to the left of $\rho_{lm}^{(0)}$, those to the right of $\rho_{lm}^{(0)}$, and the relative time ordering of the dummy time variables of integration t_j on the left side of the diagram with respect to the t_j' on the right side of the diagram. In total, there are n interactions: k to the left of $\rho_{lm}^{(0)}$ and $n-k$ to the right of $\rho_{lm}^{(0)}$. Thus, in addition to time ordering, k can run from 0 to n and provide additional terms to the density-operator element $\rho^{(n)}$.

A term of Eq. (2) is conveniently represented in graphical form as shown in Fig. 1. The time axis is in the vertical direction. To the left of the time axis, the interaction sequence to the left of $\rho_{lm}^{(0)}$ (ket evolution) is indicated, and to the right of the time axis, the interaction sequence to the right (bra evolution) of $\rho_{lm}^{(0)}$. The selection of k specifies the number of the n interactions which occur on the ket, the remaining $n-k$ interactions are then associated with the bra evolution. With the adoption of the graphical representation, the enumeration of the processes contributing to the nth-order term becomes (a) selection of k, the number of interaction vertices out of n which occur on the ket, and (b) selection of the relative time ordering of the interaction points on the left-hand side of the diagram in relation to the ordering of the $n-k$ interaction points on the right-hand side of the diagram. This corresponds to a selection of one

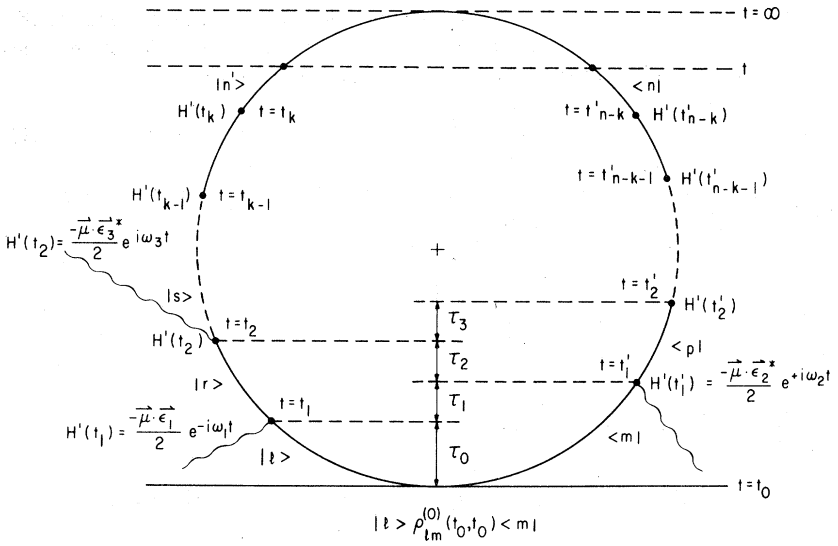

FIG. 1. Diagrammatic representation of one of the nth-order density operator elements. The left-hand side of the time axis represents the evolution of the wave function perturbed by $H'(t_1), H'(t_2), \ldots, H'(t_k)$ at $t_1, t_2, \ldots, t_k$, respectively. The right-hand side of the time axis represents the evolution of its complex conjugate perturbed by $H'(t'_1), H'(t'_2), \ldots, H'(t'_{n-k})$ at $t'_1, t'_2, \ldots, t'_{n-k}$, respectively. Specific photon absorption and emission operations have been chosen in accordance with Fig. 2.

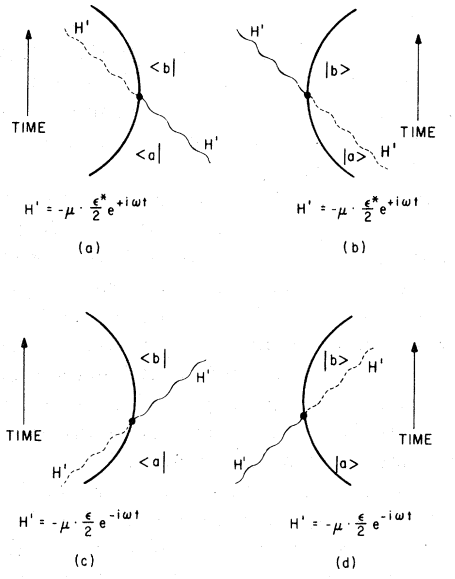

FIG. 2. Fundamental radiative perturbations of the bra and ket by photon fields. The solid wavy lines in (a) and (c) represent "negative"-energy photon annihilation $e^{-i(-\omega)t}$ and creation operations, respectively, and the dotted wavy line represents "positive"-energy photon creation and annihilation operations, respectively, acting on a bra. Each perturbation term has two algebraically equivalent interpretations depending upon whether "positive"- or "negative"-energy photon interpretations are chosen. Similarly, in (b) and (d) the solid lines correspond to a "positive"-energy photon interpretation and the dotted lines to a "negative"-energy photon interpretation. To maintain simplicity and conform to the notation used by previous authors for transition rate calculations (Refs. 1–4), we use negative energy for the bra interactions and positive energy for the ket interactions (solid wavy line).

of the time-ordered arrangements of the unit step functions included inside the P (or time-ordering) operator. For any choice of P, the number of individual time-ordered possibilities is $n!/k!(n-k)!$. The simplest case, that of $k=0$, has only one contributing diagram.

Although the vertices (dots at which the interaction occur) can represent the action of an arbitrary perturbation $[H'(t_j)$ for the vertex at $t_j]$, of particular interest in nonlinear optics are vertices of single-photon absorption and emission operations in the dipole approximation. These are represented by the standard notation shown in Fig. 2 for emission and absorption operations on the bra and ket. t refers to the time associated with the dot (integration variable). The dipole interaction is chosen to be specific, and can be replaced by other absorption processes. In these representations ϵ or ϵ^* can be an arbitrary function of time to thus represent a pulsed field. As pointed out in Fig. 2, we shall uniformly use solid wavy lines to represent the perturbation interactions.

III. INCLUSION OF DAMPING AND LINEWIDTH

Damping and linewidth are included in the present formalism, in a manner similar to that discussed by Omont, Smith, and Cooper,[5] through the statistical average indicated in Eq. (2). Referring to Fig. 1, tracing up the two sides in time, linewidths are associated with the dephasing of superposition states created by the absorption or emission field operations. Thus, for example, the interaction at $t=t_1$ causes the ket to evolve into a

state $|r\rangle$, while the bra remains in state $\langle m|$. The off-diagonal density-matrix element resulting from this photon interaction at t_1, ρ_{rm}, decays as a function of time after the interaction at t_1. This decay is subsequently interrupted by the photon interaction at $t = t_1'$, which throws the bra into the state $\langle p|$, whereupon the corresponding density-matrix element ρ_{rp} decays as a function of time subsequent to $t = t_1'$.

If at any time both the bra and the ket refer to the same state on the diagram, the time evolution is that of a diagonal component of the density matrix, and the decay of this diagonal component describes a populational decay.

This treatment of damping is well known from the theory of scattering processes and will be included here in an identical manner, and in enough detail to establish the usual damping terms associated with the density matrix. Much work has been done in relation to collisional theory,[10] and is important in considering many optically nonlinear interactions.

A basis for the introduction of damping is provided by first of all considering the ideal case for which damping and linewidth are neglected. $K^+(x_{q+1}, x_q)$ then is simply the retarded Green's function for the freely propagating ket.[11]

$$K^+(t_{q+1}, t_q) = \sum_n \exp[-i\omega_n(t_{q+1} - t_q)]\,|\phi_n\rangle\langle\phi_n| \quad (3a)$$

and

$$K^-(t_j', t_{j+1}') = [\,K^+(t_{j+1}', t_j')]^* . \quad (3b)$$

We thus observe that for this situation the K^+ and K^- factors are independent of the time ordering in Eq. (2). Thus, each of the time-ordered terms has the same integrand except for the time-ordered unit-step factors. However, the sum of the individual terms in $P[U(t-t_k)U(t_k-t_{k-1})\cdots]$ gives a single term:

$$\begin{aligned} &P[U(t-t_k)U(t_k-t_{k-1})\cdots] \\ &\quad = [U(t-t_k)U(t_k-t_{k-1})\cdots U(t_1-t_0)] \\ &\qquad \times [U(t-t_{n-k}')U(t_{n-k}'-t_{n-k-1}')\cdots U(t_1'-t_0)], \end{aligned} \quad (3c)$$

which is a product of the two independent factors contained in the square brackets which involve the wave function and its complex conjugate, respectively. Thus, the evolution of the bra side of the diagram is, in this ideal case, independent of the evolution of the ket side of the diagram when all the time-ordered $n!/(k-n)!k!$ possibilities are taken into account. This also implies that, in conventional density-matrix analysis, $n!/(k-n)!k!$ terms would be deduced which, if summed, would provide a single simplified term. Although more naive, in this case it is less laborious not to directly calculate the density matrix but to calculate the evolution of the wave function and its complex conjugate independently and subsequently obtain the density matrix. The individual time orderings which automatically arise in the density matrix would be avoided. Examples of such a simplification are provided later.

These non-time-ordered situations can also be handled diagrammatically by the approach developed by Ward[2]; however, the individual time-ordered contributions are lost.

On the other hand, when damping and coherence loss are included, the relative time ordering of the vertices associated with the bra and ket cannot be avoided and the previous diagrammatic approaches, for which such a time ordering is not included, are insufficient.

The importance of time ordering arises because K^+ and K^- in the statistical average of Eq. (2) cannot be independently specified since it is the density-matrix element which decays. K^+ and K^- are no longer given by Eqs. (3a) and (3b). It is, in addition, possible that, due to a collision, the bra and ket might suffer important transitions, in which case the operators K^+ and K^-, or the combination of them, could have significant off-diagonal matrix elements.

The proper introduction of damping is performed by considering the matrix elements of operator $\hat{K}(t_2, t_1) = K^+(t_2, t_1)K^-(t_1, t_2)$ in the sense

$$\begin{aligned} \langle\langle aa'\,|\hat{K}(t_2, t_1)\,|bb'\rangle\rangle &= \langle a\,|K^+(t_2, t_1)\,|b\rangle \\ &\quad \times \langle b'\,|K^-(t_1, t_2)\,|a'\rangle , \end{aligned} \quad (4)$$

where $t_2 - t_1$ is the time interval between two interaction vertices (Fig. 1). In the impact approximation[5,10] t_2 and t_1 enter as $t_2 - t_1$, and $K^+(t_2, t_1)$ can be written as $K^+(t_2, t_1')K^+(t_1', t_1)$, where

$$t_2 - t_1 = t_2 - t_1' + t_1' - t_1 .$$

Thus, one observes from Fig. 1 that the K^+K^- factors in Eq. (2) can be written as a product of

$$\cdots\hat{K}(t_2, t_1')\hat{K}(t_1', t_1)\hat{K}(t_1, t_0) = \cdots\hat{K}(\tau_2)\hat{K}(\tau_1)\hat{K}(\tau_0)$$

factors with $\tau_0, \tau_1, \ldots$ indicated in Fig. 1. Since $\tau_1, \tau_2, \ldots$ are independent parameters, the statistical average of the products is the product of the statistical averages and one thus obtains factors of the form

$$\langle\langle aa'\,|\hat{A}(\tau)\,|bb'\rangle\rangle = \langle\langle aa'\,|[K(t_2 - t_1)]_{\rm av}\,|bb'\rangle\rangle , \quad (5)$$

where the $\hat{A}(\tau)$ operators are familiar from the theory of line broadening.[5,10] In the so-called isolated-line approximation,[5,10] these operators have been shown to have diagonal matrix elements (for a nondegenerate system) of the form

$$\langle\langle ab|\hat{A}(\tau)|a'b'\rangle\rangle = \delta_{aa'}\delta_{bb'}\exp(-i\omega_{ab}\tau - \phi_{ab}\tau), \quad (6a)$$

where

$$\phi_{ab} = \phi_{ba}^{*} = \gamma_{ab} + i\Delta_{ab}, \quad (6b)$$

$$\gamma_{ab} = \gamma_{ab}^{c} + \tfrac{1}{2}(\Gamma_a + \Gamma_b), \quad (6c)$$

$$\phi_{aa} = \gamma_a = \gamma_a^{c} + \Gamma_a, \quad (6d)$$

and $1/\Gamma_a$ is the natural lifetime of level a; γ_a^c is the inelastic collision frequency for level a. The terms γ_{ab}^c and Δ_{ab} account for collisional broadening and frequency shifts.

With these matrix elements, Eq. (2) can be expressed in terms of integrals over $\tau_1, \tau_2, \ldots$, and simple rules can be deduced by which to obtain steady-state susceptibilities. We demonstrate this change of variables and the introduction of appropriate matrix elements of the $\hat{K}(\tau)$ operators and the perturbation Hamiltonian for times up to t_2. From Eq. (2) and Fig. 1, one has under the time integrals

$$K^{+}(t_2, t_1)H'(t_1)K^{+}(t_1, t_0)|l\rangle\rho_{lm}^{(0)} \times \langle m|K^{-}(t_0, t_1')H'(t_1')K^{-}(t_1', t_2), \quad (7a)$$

which becomes

$$K^{+}(\tau_2)K^{+}(\tau_1)H'(t_1' - \tau_1)K^{+}(\tau_0)|l\rangle\rho_{lm}^{(0)}(t_0) \times \langle m|K^{-}(\tau_0)K^{-}(\tau_1)H'(t_2 - \tau_2)K^{-}(\tau_2). \quad (7b)$$

Assuming that upon the interactions $H'(t_1)$ and $H'(t_1')$ the system enters the states indicated on the diagram (Fig. 1), one has, upon averaging,

$$\begin{aligned}|r\rangle\langle r|K^{+}(\tau_2)|r\rangle\langle r|K^{+}(\tau_1)|r\rangle\langle r|H'(t_1' - \tau_1)|l\rangle\langle l|K^{+}(\tau_0)|l\rangle\rho_{lm}^{(0)}(t_0)\langle m|K^{-}(\tau_0)|m\rangle\langle m|K^{-}(\tau_1)|m\rangle \\ \times\langle m|H'(t_2 - \tau_2)|p\rangle\langle p|K^{-}(\tau_2)|p\rangle\langle p| \\ = |r\rangle\langle p|\rho_{lm}^{(0)}(t_0)\langle\langle rp|\hat{A}(\tau_2)|rp\rangle\rangle\langle\langle rm|\hat{A}(\tau_1)|rm\rangle\rangle\langle\langle lm|\hat{A}(\tau_0)|lm\rangle\rangle\langle r|H'(t_2 - \tau_2 - \tau_1)|l\rangle\langle m|H'(t_2 - \tau_2)|p\rangle . \quad (7c)\end{aligned}$$

Thus it is seen that Eq. (2) can be written in the form

$$\begin{aligned}\rho^{(n)}(t, t) = \sum_{lm}\int_{t-t_0-\tau_2-\tau_3-\cdots}^{0} d(-\tau_1)\int_{t-t_0-\tau_3-\cdots}^{0} d(-\tau_2)\cdots\langle\langle rp|A(\tau_2)|rp\rangle\rangle \\ \times\langle m|H'(t-\tau_2-\tau_3-\cdots)/-i\hbar|p\rangle\langle\langle rm|\hat{A}(\tau_1)|rm\rangle\rangle \\ \times\langle r|H'(t-\tau_1-\tau_2-\cdots)/i\hbar|l\rangle\langle\langle lm|\hat{A}(t-\tau_1-\tau_2\cdots-t_0)|lm\rangle\rangle \\ \times\rho_{lm}^{(0)}(t_0)|r\rangle\langle p|\cdots . \quad (8)\end{aligned}$$

This expression is thus *one* of the possible time-ordered terms indicated in Eq. (2) and shown explicitly in Fig. 1. It is a simple generalization of the Van Kranendonk-Fiutak equation for the calculation of transition rates and is formally identical to the response-function formalism in nonlinear optics.[12]

IV. CALCULATIONAL RULE FOR THE POLARIZATION OF MONOCHROMATIC FIELDS

Taking as a specific case absorption at frequency ω_1 at t_1 and absorption at frequency ω_2 at t_1', assuming also the dipole approximation, $H'(t_1) = -\frac{1}{2}(\vec{\mu}\cdot\vec{\epsilon}_1)\times e^{-i\omega_1 t_1}$, $H'(t_1') = -\frac{1}{2}(\vec{\mu}\cdot\vec{\epsilon}_2^{*})e^{+i\omega_2 t_1'}$. Also, using Eq. (6) for the matrix elements of the $\hat{A}$ operators in Eq. (8), we consider the integrations over τ_1 and τ_2. For the initial conditions we shall set

$$\rho_{lm}^{(0)}(t_0)\exp[+i(\omega_{lm} - i\phi_{lm})t_0] = \rho_{lm}^{(0)} .$$

For most cases of interest, the nondiagonal components are initially zero and the diagonal components assume a statistical distribution. However, it is useful at this point to include the possibility of an initially nonzero decaying polarization. To extract the steady-state value we take the limit as $t_0 \to -\infty$ and assume diagonal matrix elements for $A(\tau_1)$ and $A(\tau_2)$ to obtain

$$\begin{aligned}\rho^{(n)}(t, t) = \cdots\int_{+\infty}^{0} d(-\tau_4)\int_{+\infty}^{0} d(-\tau_3)\frac{|r\rangle\exp[-i\omega_1(t-\tau_3-\cdots)]}{\hbar(\omega_1 - \omega_{rm} + i\phi_{rm} + \omega_{lm} - i\phi_{lm})}\langle r|-\vec{\mu}\cdot\tfrac{1}{2}\vec{\epsilon}_1|l\rangle \\ \times\rho_{lm}^{(0)}\langle m|-\vec{\mu}\cdot\tfrac{1}{2}\vec{\epsilon}_2^{*}|p\rangle\frac{\exp[+i\omega_2(t-\tau_3-\cdots)]}{-\hbar(\omega_1 - \omega_2 - \omega_{rp} + i\phi_{rp} + \omega_{lm} - i\phi_{lm})} \\ \times\langle p|\cdots\exp[-i(\omega_{lm} - i\phi_{lm})(t-\tau_3-\cdots)] . \quad (9)\end{aligned}$$

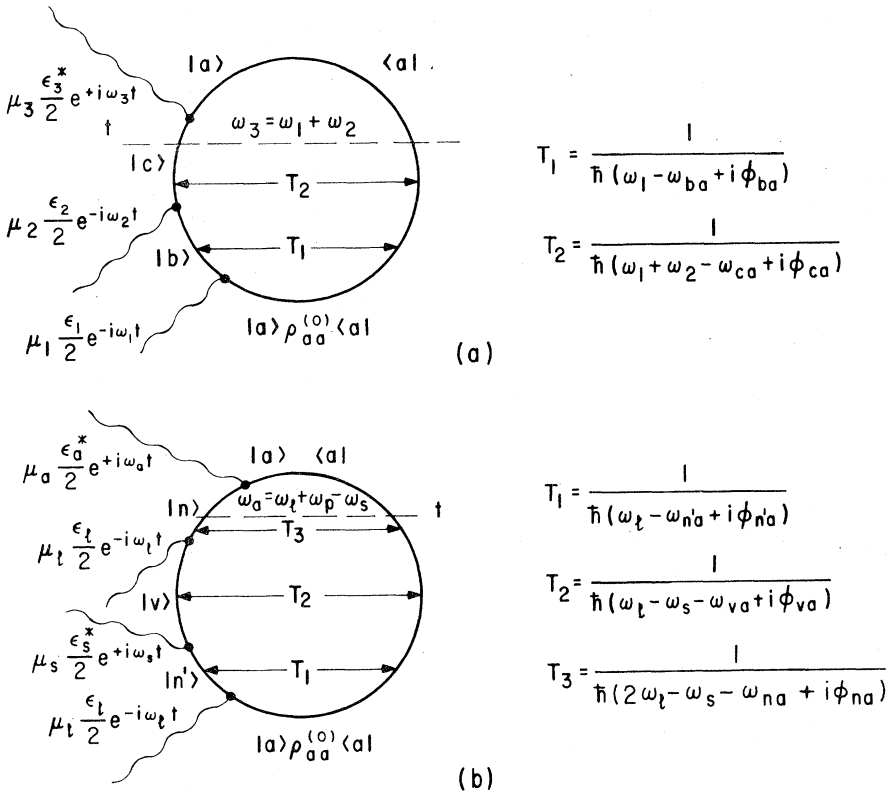

FIG. 3. Basic density-operator diagrams for (a) resonant sum frequency generation and (b) resonant coherent anti-Stokes Raman scattering. We consider the evaluation of polarization at time t indicated on the diagrams. The propagators T_n's in each case have been obtained by applying the rules below Eq. (9).

This is sufficient to extract the general rule for obtaining the susceptibility once the diagram is specified. As can be seen from this equation the rules are the following:

(i) A factor of $\rho_{lm}^{(0)}$ the initial value of the density-matrix element.

(ii) Following the diagram in time multiply by the matrix element of the first interaction, in this case $\langle r| - \frac{1}{2}(\vec{\mu} \cdot \vec{\epsilon}_1)|l\rangle$, the coupling which brings the system from state $|l\rangle$ to $|r\rangle$.

(iii) Propagate to next interaction vertex by multiplying by the propagator. This is given by ± the inverse of (a) the sum of photon energies corresponding to the absorption operations up to and including the interaction referred to in (ii), (b) minus the sum of photon energies corresponding to the emission operations up to and including the interaction referred to in (ii),[13] (c) minus $\hbar$ times the transition frequency of the superposition state which the system enters as a result of the interaction in (ii), and (d) plus $\hbar$ times the complex transition frequency of the initial superposition state. The complex frequency is equal to $\omega_{ij} - i\phi_{ij}$, where $\omega_{ij} = \omega_i - \omega_j$ where i represents the ket and j the bra at the time of evaluation. The minus sign in front of the propagator is taken if the interaction which just occurred was on the right (bra) side of the diagram and the plus sign if it was on the ket side. Thus, in the present case, after the first interaction [referred to in (ii)] the appropriate propagator is

$$[\hbar(\omega_1 - \omega_{rm} + i\phi_{rm} + \omega_{lm} - i\phi_{lm})]^{-1}.$$

(iv) Repeat (ii) to (iii) with each subsequent interaction and propagation. This brings in the additional coupling factor and propagators shown in Eq. (9).

(v) Proceed up the diagram to time t, the time desired; the last factor being a propagator from step (iii).

(vi) Multiply by the frequency factor $\exp[-i(\omega_1 - \omega_2 + \cdots + \omega_{lm} - i\phi_{lm})t]$, as obtained from the conservation of energy[13] at each vertex. The factor $e^{-i\phi_{lm}t}$ arises from an initially decaying superposition state. Its interpretation will become clear in Secs. V and VI.

(vii) Multiply by $|n'\rangle\langle n|$ to obtain the density operator at time t.

In this section, we consider some of the basic nonlinear optical susceptibilities which are well known but demonstrate the utility of the diagrammatic approach. For these we take $\rho_{lm}^{(0)} = \delta_{lm}\rho_{ll}^{(0)}$ and $\omega_{ll} - i\phi_{ll} = 0$.

The simplest diagram is that for harmonic generation [Fig. 3(a)] or parametric conversion which has no counter-rotating resonances and for which

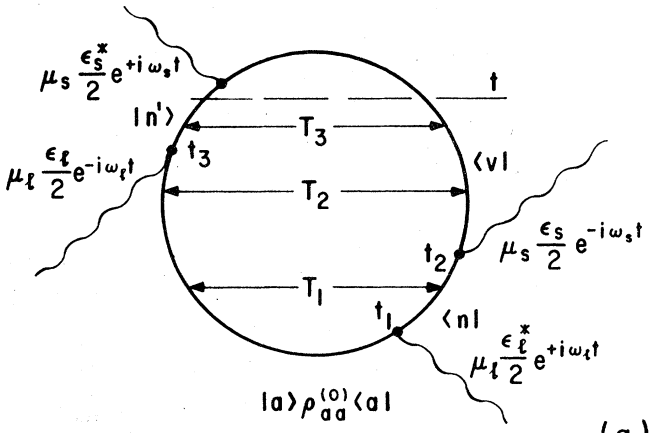

$$T_1 = \frac{-1}{\hbar(-\omega_\ell - \omega_{an} + i\phi_{an})}$$

$$T_2 = \frac{-1}{\hbar(-\omega_\ell + \omega_s - \omega_{av} + i\phi_{av})}$$

$$T_3 = \frac{+1}{\hbar(+\omega_s - \omega_{n'v} + i\phi_{n'v})}$$

$$T_1 T_2 T_3 = T^{(1)}$$

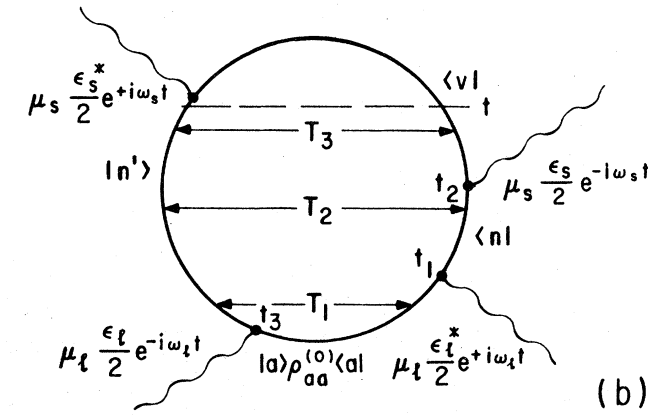

$$T_1 = \frac{+1}{\hbar(+\omega_\ell - \omega_{n'a} + i\phi_{n'a})}$$

$$T_2 = \frac{-1}{\hbar(-\omega_{n'n} + i\phi_{n'n})}$$

$$T_3 = \frac{-1}{\hbar(+\omega_s - \omega_{n'v} + i\phi_{n'v})}$$

$$T_1 T_2 T_3 = T^{(2)}$$

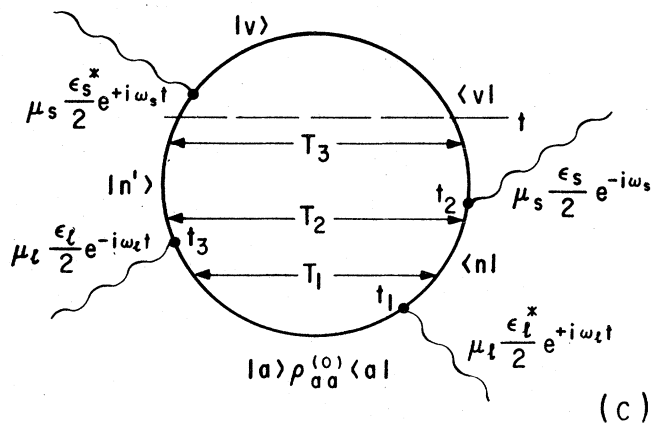

$$T_1 = \frac{1}{\hbar(\omega_\ell + \omega_{an} - i\phi_{an})}$$

$$T_2 = \frac{1}{\hbar(-\omega_{n'n} + i\phi_{n'n})}$$

$$T_3 = \frac{-1}{\hbar(+\omega_s - \omega_{n'v} + i\phi_{n'v})}$$

$$T_1 T_2 T_3 = T^{(3)}$$

FIG. 4. Three time-ordered diagrams for the Raman effect. (a) Vibrationally resonant term, (b) and (c) the hot luminescence terms of Shen (Ref. 21).

only one state is significantly populated. Time ordering does not enter since the interactions occur on one side of the diagram and the present approaches reduce essentially to previous diagrammatic techniques. The diagram indicates one path through the system which contributes to the second-harmonic polarization. From the diagram, applying the above rules, the density operator at

time t is

$$\rho(t,t) = \exp[-i(\omega_1+\omega_2)t]|c\rangle\, T_2\langle c|-\vec{\mu}\cdot\tfrac{1}{2}\vec{\epsilon}_2|b\rangle T_1 \times\langle b|-\vec{\mu}\cdot\tfrac{1}{2}\vec{\epsilon}_1|a\rangle\rho_{aa}^{(0)}\langle a|. \quad (10)$$

Figure 3(b) indicates the significant diagram for totally resonant coherent anti-Stokes Raman scattering[14-20] $|n'\rangle$, to be specific, is an electronic level, $|v\rangle$ the vibrational level, ω_l the laser frequency, ω_s the Stokes frequency, and ω_a the anti-Stokes frequency. This is the only contributing diagram (density-matrix element) if (i) ω_l and ω_s are close to resonance, (ii) $|a\rangle$ is the only significantly populated level, (iii) $\omega_l-\omega_s$ is close to the vibrational resonance. As will be seen, if the electronic resonances are not guaranteed and ρ_{aa} is not the only significant term, other density-matrix elements become significant.[20] From the diagram at time t

$$\rho(t,t) = \tfrac{1}{8}(\epsilon_l)^2\epsilon_s^* e^{-i\omega_a t}|n\rangle\, T_3\langle n|-\mu_l|v\rangle T_2 \times\langle v|-\mu_s|n'\rangle\, T_1\langle n'|-\mu_l|a\rangle\rho_{aa}^{(0)}\langle a|, \quad (11)$$

where ϵ_l and ϵ_s are the laser and Stokes field amplitudes, respectively, and μ_l and μ_s are the projections of the dipole operator along the directions of the respective fields.

The diagrams shown in Fig. 4 are those providing the polarization of the Raman effect, stimulated or spontaneous according to the stimulated or spontaneous character of the field ϵ_s. At t, the density-matrix element has the Stokes frequency ω_s $(=\omega_l-\omega_l+\omega_s)$; however, in contrast to the previous cases, there are three time-ordered possibilities: Figure 4(a) $t_3>t_2>t_1$, 4(b) $t_2>t_1>t_3$, and 4(c) $t_2>t_3>t_1$. Each one of these three corresponds to a term contributing to the density-matrix element $\rho_{n'v}$. Three perturbation terms thus arise from conventional density-matrix analysis.[21] The three density operator elements at time t are given by

$$\rho(t,t) = |n'\rangle\langle n'|-\tfrac{1}{2}\mu_l\epsilon_l|a\rangle\rho_{aa}^{(0)}\langle a|-\tfrac{1}{2}\mu_l\epsilon_l^*|n\rangle \times\langle n|-\tfrac{1}{2}\mu_s\epsilon_s|v\rangle\langle v|T_1T_2T_3e^{-i\omega_s t}, \quad (12a)$$

where the propagators T_1, T_2, and T_3 are shown in Fig. 4 for each time-ordered case. Figure 4(a) has the vibrationally resonant denominator and two electronic resonances; one terminating at the ground state and one terminating at the vibrational state. Figure 4(a) is the most significant term and is the usual off-resonance Raman susceptibility.[1] The other two diagrams have no vibrational resonance, but become significant when ω_l is close to an electronic-transition frequency. For $n=n'$ and for time t' such that $t_1<t'<t_2$ and $t_3<t'<t_2$, respectively, for these two diagrams, one observes that the diagonal density matrix $\rho_{n'n'}$ enters into the perturbation and exhibits a linewidth (or transient decay) associated with the lifetime of level n'. These two diagrams for transient excitation at ω_l and a monochromatic excitation at the Stokes frequency ω_s provide the terms attributed to hot luminescence by Shen[21]; the first diagram provides the transient-Raman-scattering term.[7,21]

Summing of the time-ordered diagrammatic contributions when broadening and lifetime are neglected can be readily performed for these three time-ordered diagrams for the Raman effect. From Fig. 4 the sum of the products of the propagators $T^{(1)}+T^{(2)}+T^{(3)}=T^{(t)}$, which is seen to reduce to a product of three propagators and thus the density-matrix operator can be written (Fig. 5)

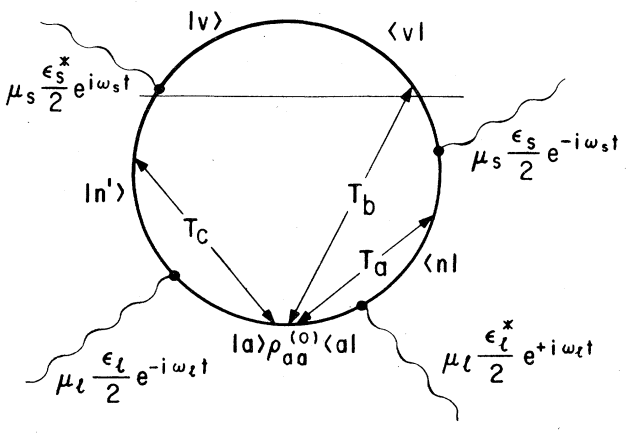

$$T_a = \frac{1}{\hbar(\omega_l-\omega_{na})}$$

$$T_b = \frac{1}{\hbar(\omega_l-\omega_s-\omega_{va})}$$

$$T_c = \frac{1}{\hbar(\omega_l-\omega_{n'a})}$$

$$T^{(1)}+T^{(2)}+T^{(3)} = T^{(t)} = T_aT_bT_c$$

FIG. 5. Non-time-ordered calculation of the Raman susceptibility. This can be obtained by summing the diagrams of Fig. 4 or using the propagators for the independent evolution of the bra and ket (Ref. 22).

$$\rho(t,t) = \frac{|n'\rangle\langle n'|-\mu_1|a\rangle\rho_{aa}^{(0)}\langle a|-\mu_1|n\rangle\langle n|-\mu_s|v\rangle\langle v|}{\hbar(\omega_1-\omega_{n'a})\hbar(\omega_1-\omega_{na})\hbar(\omega_1-\omega_s-\omega_{va})} \times \tfrac{1}{8}|\epsilon_1|^2\epsilon_s e^{-i\omega_s t}. \quad (12b)$$

This is simply the product of (i) the density-matrix element for the initial state, (ii) the propagator for the left-hand side of the diagram, (iii) the product of the two propagators for the right-hand side of the diagram, and (iv) the appropriate matrix elements for the interactions. This ability to sum is a particular example of the general results implied by Eq. 3(c). This also shows that if linewidth and decay are neglected it is less laborious to obtain the total susceptibility by a separate perturbation analysis of the wave function and its complex conjugate, since each time-ordered factor is obtained from the density-matrix analysis. We see, comparing Eqs. (12a) and (12b), that when the two diagrams Figs. 4(b) and 4(c) are added to that of Fig. 4(a) the electronic resonance $\omega_s-\omega_{n'v}$ is changed to $\omega_1-\omega_{n'a}$ and hence can be important although it is small. We observe also that Eq. 12(b) has transition frequencies only to the initial state as a consequence of the independent evaluation by propagators of the ket and bra.[22] This is characteristic of previous propagator applications to the calculations of nonlinear optical polarizations.[2]

Figure 6 illustrates the terms contributing to Eq. (2-29) in Ref. 1 for the particular case of second-harmonic generation. $\rho(t,t)$ is of the form

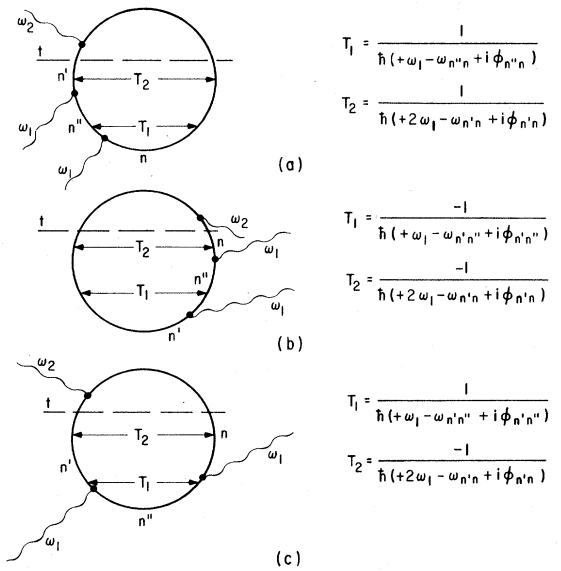

FIG. 6. Second-harmonic generation diagrams corresponding to Eq. (2-29) of Ref. 1.

$$\rho(t,t) = |n'\rangle\langle n'|-\vec{\mu}\cdot\tfrac{1}{2}\vec{\epsilon}|n''\rangle\langle n''|-\vec{\mu}\cdot\tfrac{1}{2}\vec{\epsilon}|n\rangle \times\langle n|T_1T_2e^{-i2\omega_1 t}\rho_{kk}^{(0)}, \quad (13)$$

with T_1 and T_2 the propagators defined on the individual diagrams, and $k=n$, n', and n'' for the three diagrams, respectively. $\vec{\epsilon}$ is the electric field of the fundamental. Figure 6(a) is that of Fig. 3(a) and provides the resonant terms proportional to the initial ground-state population. The second and third diagrams provide the resonant terms proportional to the upper level and intermediate populations, $\rho_{n'n'}^{(0)}$ and $\rho_{n''n''}^{(0)}$, respectively. The two further time-ordered contributions of Fig. 6(c) provide the two additional factors proportional to $\rho_{n''n''}^{(0)}$ in Ref. 1.

We would, finally, like to consider in greater detail a diagrammatic analysis of lowest-order Raman anti-Stokes scattering which involves a laser field of amplitude ϵ_1 at frequency ω_1, a Stokes field of amplitude ϵ_s at frequency ω_s, and an anti-Stokes field ϵ_a at frequency ω_a generated through the mixing of ϵ_1 and ϵ_s with a resonant mode of the medium.[14-19]

We consider those terms proportional to the ground-state population providing the polarization components at ω_1, ω_s, and ω_a, respectively. Only the coherent anti-Stokes process will be considered. Thus stimulated Raman scattering, for example, will be neglected. Since the evaluation of the polarization from the rules is straightforward, it suffices for this discussion to investigate the diagrammatic contributions.

For the generation of photons at ω_1 by those at ω_s and ω_a, there are 48 possible diagrams. The four basic ones are given in Figs. 7(a) and 7(b). The two diagrams of Fig. 7(a) have three time-ordered possibilities, thus increasing this to eight fundamental diagrams. The 48 diagrams are thus obtained by permuting the three vertices of each of these eight fundamental diagrams. In the permutation operations, the slopes of all photon lines must be arranged in the way that the frequency of the polarization is preserved.

The four basic diagrams (eight including time-ordering) contributing to the polarization at frequency ω_s due to the fields at ω_a and ω_1 are shown in Figs. 7(c) and 7(d). These are doubled by interchanging vertices 1 and 2 and are also doubled by interchanging 1 and 3. These, however, cannot be doubled a second time because an interchange of the ω_1 photons is canceled by the Bose-Einstein statistics. Thus with the time ordering considered there is a possibility of 24 diagrams or density matrix terms.

Similarly, for the generation of photons at ω_a, the contributing graphs are given by Figs. 7(e) and

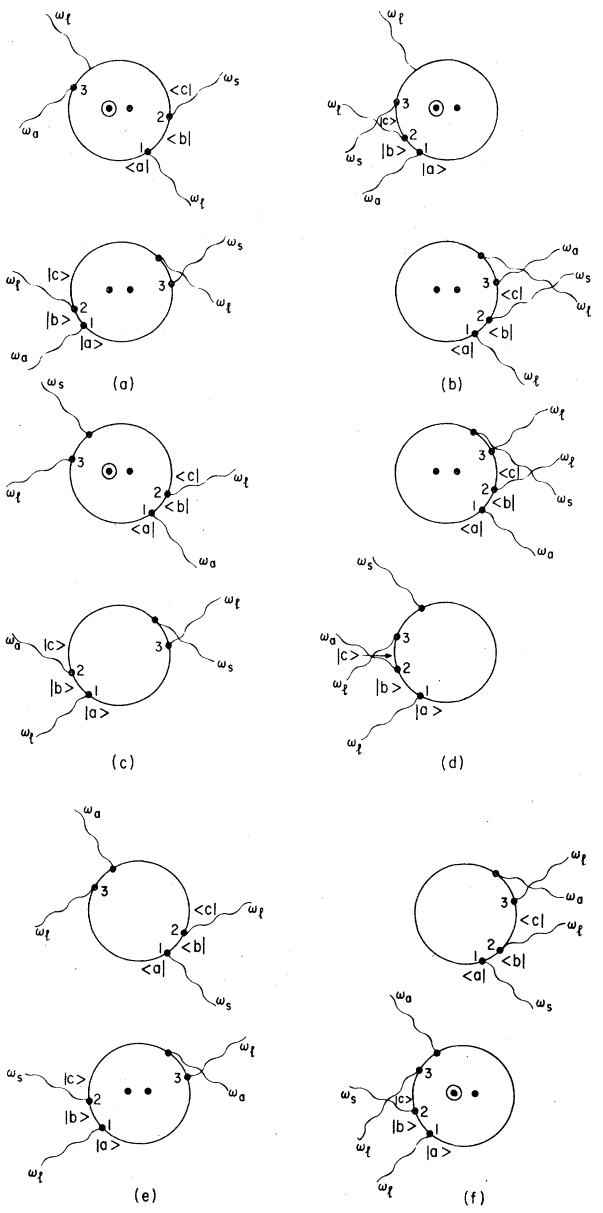

FIG. 7. Diagrammatic representations for coherent anti-Stokes Raman scattering. (a) and (b) are the four basic diagrams for the generation (absorption) of photons at ω_l due to the presence of the fields at frequencies ω_s and ω_a. (c) and (d) are the four basic diagrams for the generation (absorption) of Stokes photons at ω_s by the fields at ω_l and ω_a. (e) and (f) represent the generation (absorption) of anti-Stokes photons at ω_a by the fields at ω_l and ω_s.

7(f) and the exchange diagrams with respect to vertices 1 and 2 and 1 and 3. A total of 24 diagrams is possible.[20,23]

One observes that the two time-ordering possibilities not explicitly shown [corresponding to Figs. 4(b) and 4(c) for the nonparametric diagrams] are those which give the two-photon resonance denominators, which do not have a ground-state vibrational resonance. These terms can contribute to X_{NR}, the off-vibrational resonance portion of the susceptibility; however, as seen earlier, these small terms can contribute to a shift in the electronic resonances of the time-ordered diagram shown with the vibrational resonance, and hence can be important.[19,20]

For off-resonant excitation all of the diagrams of Fig. 7 must be considered. For near-vibrational resonance, considering only the vibrationally resonant part of the susceptibility X_R, the diagrams indicated by a central dot contribute significantly (rotating-wave approximation). The second dot signifies the inclusion of the exchange diagrams with respect to vertices 1 and 2. (In addition, the time orderings not shown explicitly are excluded.) If counter-rotating contributions can be discriminated at both electronic and vibrational resonances, only the diagrams with the central circles need be considered; two diagrams at frequency ω_l and one each at ω_s and ω_a are then important.

For ϵ_a initially zero, the only polarization of interest is that at frequency ω_a (ϵ_l and ϵ_s are assumed constant). As is apparent from Fig. 7(e) and 7(f), this coherent generation of anti-Stokes radiation by both the lossless and lossy part of the susceptibility, which has been treated in detail,[14-19] has 24 contributing density-matrix elements involving the ground-state population alone. Additional terms arising from excited-state populations can also contribute significantly, 24 possible graphs for each excited state population, or a possible total of 96. Since the vibrationally nonresonant contributions provide terms to the nonresonant background susceptibility that can be of importance in the detection process, these, in general, cannot be ignored.

V. CALCULATIONS FOR PULSED FIELDS

Pulsed fields in contrast to monochromatic excitation allow a diversity of interactions for which no simple general calculational rules are possible. The diagrammatic representation of the terms of Eq. (2) are nonetheless unambiguous and thus are more advantageous than energy level diagrams. There are also specific transient excitations and responses for which the derivation of rules is of enough generality to be useful. This is true of the pulse-excitation–pulse-probe techniques for which strong excitation pulses initiate a transient response which is probed generally later in time by a weak probing pulse. As will be seen, consider-

able insight and ease of calculation is attained with the diagrammatic approach. In the present section, we consider first the derivation of the computational rules for third-order perturbation followed by a specific application to coherent transient birefringence.

Three basic simplifying assumptions will be made which eliminate complicating transient responses which, experimentally, are either weaker than the coherent transient response to be discussed or can be separated from it. These assumptions are the following: (a) The time variation of the complex amplitude $\epsilon_1(t)$ constitutes an adiabatic change with respect to the first transition. (b) The time variation of the complex amplitude of the probe field is adiabatic with respect to the transition brought about at the third vertex. (c) The probe field is temporally separated from the exciting field.

We consider then coherent interactions for which the first two interaction vertices arise from strong excitation pulses; these two vertices can be on either side of the diagram. Using Fig. 1 once again as the specific time-ordered example, one integrates Eq. (8) by parts over τ_1. This integral is then given by

$$
\begin{aligned}
&-\int_{+\infty}^{0} \exp(-i\omega_{rm}\tau_1 - \phi_{rm}\tau_1)\,|r\rangle\langle r| - \frac{\vec{\mu}\cdot\vec{\epsilon}_1(t-\tau_1-\cdots)}{2i\hbar}\,|m\rangle \exp[-i\omega_1(t-\tau_1-\tau_2-\cdots)]\,d\tau_1\,\rho_{mm}^{(0)}\langle m| \\
&\quad = \exp[-i\omega_1(t-\tau_2-\cdots)][+1/\hbar(\omega_1-\omega_{rm}+i\phi_{rm})]\,|r\rangle\langle r| - \vec{\mu}\cdot\tfrac{1}{2}\vec{\epsilon}_1(t-\tau_2-\cdots)\,|m\rangle\,\rho_{mm}^{(0)}\langle m| \\
&\quad\quad - \int_{+\infty}^{0} \frac{\exp[-i(\omega_{rm}-\omega_1)\tau_1 - \phi_{rm}\tau_1 - i\omega_1(t-\tau_2-\cdots)]}{2\hbar(-\omega_{rm}+i\phi_{rm}+\omega_1)}\,|r\rangle\langle r| - \vec{\mu}\cdot\frac{\partial\vec{\epsilon}_1}{\partial\tau_1}\,|m\rangle\,d\tau_1\,\rho_{mm}\langle m|\,, \qquad (14a)
\end{aligned}
$$

where we have taken $\rho_{lm}^{(0)} = \rho_{mm}^{(0)}\delta_{lm}$.

Assumption (a) above implies the retention of only the first term in the above expression. This assumes that $|\partial\vec{\epsilon}_1/\partial\tau_1| \ll |(\omega_{rm}-\omega_1+i\phi_{rm})|$. Since the first transition is assumed to be electronic, this assumption is valid far off of the resonant excitation. As an electronic resonance is approached, however, if the lifetime is longer than the pulse, transient polarization decay must be considered. Thus, for pulses of the order of a picosecond, the analysis of the coherent effects discussed here are strictly expected to be valid for the constraints $\omega_{rm}-\omega_1 \gg 10^{12}$ or $\phi_{rm} \gg 10^{12}$. These assumptions are equivalent to those requiring an instaneous response from the first transition.

At the second vertex, for which the field interaction arises from the strong pulses (Fig. 1), one has the integral over τ_2 which can be written

$$
\begin{aligned}
&-\int_{+\infty}^{0} d\tau_2 \exp[-i\omega_{rp}\tau_2 - \phi_{rp}\tau_2]\langle m| - \vec{\mu}\cdot\vec{\epsilon}_2^{\,*}(t-\tau_2-\cdots)\exp[i\omega_2(t-\tau_2-\cdots)]/-2i\hbar\,|p\rangle \\
&\quad\times\langle r| - \tfrac{1}{2}\vec{\mu}\cdot\vec{\epsilon}_1(t-\tau_2-\cdots)\exp[-i\omega_1(t-\tau_2-\cdots)]\,|m\rangle\,\frac{|r\rangle\rho_{mm}^{(0)}\langle p|}{\hbar(-\omega_{rm}+i\phi_{rm}+\omega_1)} \\
&\quad = \frac{1}{\hbar(-\omega_{rm}+i\phi_{rm}+\omega_1)}\exp[-(i\omega_{rp}+\phi_{rp})(+t-\tau_3+\cdots)][(\langle r|\mu_1|m\rangle\langle m|\mu_2|p\rangle)\,|r\rangle\rho_{mm}^{(0)}\langle p|\,\frac{1}{-i\hbar} \\
&\quad\quad\times\int_{-\infty}^{t-\tau_3-\cdots} \tfrac{1}{2}\epsilon_1(\xi)e^{-i\omega_1\xi}\tfrac{1}{2}\epsilon_2^{*}(\xi)e^{i\omega_2\xi}\exp[(i\omega_{rp}+\phi_{rp})\xi]\,d\xi\,, \qquad (14b)
\end{aligned}
$$

where the variable of integration has been changed to $t-\tau_2-\tau_3-\cdots$. Here also $\epsilon_1(\xi)$ and $\epsilon_2(\xi)$ are the amplitudes of $\vec{\epsilon}_1(\xi)$ and $\vec{\epsilon}_2(\xi)$ and we have taken μ_1 and μ_2, for simplicity of notation, as the components of $\vec{\mu}$ along the vector directions of $\vec{\epsilon}_1$ and $\vec{\epsilon}_2$, respectively. In obtaining Eq. (14b), we have used the absorption operation at ω_2 at the second interaction vertex. In general, the choice of either the absorption or emission operation varies from case to case, but the procedures of the calculations are the same. Thus, the present approach includes two-photon resonance and transient two-wave mixing as possibilities for establishing coherent excitation.

Equation (14b) provides the off-diagonal density-matrix element between states $|r\rangle$ and $|p\rangle$ and hence is that which provides the polarization excited by the spectrum of the field product $\epsilon_1\epsilon_2^{*}$ and associated with transitions between the excited states r and p.

To deduce the polarization associated with a probe pulse it is necessary to consider the interaction at the third vertex. With the assumption of a nonoverlap of the strong exciting pulses and a weak probe pulse, in Eq. (14b) the limit $t-\tau_3$ can be set equal to ∞ and the time dependence is simply $\exp[i(\omega_{rp}+\phi_{rp})(-t+\tau_3)]$. Thus, as is apparent from Eq. (14b), the excitation pulses prepare a decaying superposition state. Assum-

ing an adiabatic interaction for the third vertex (t_2 of Fig. 1) similar to that of the first and

$$\langle\langle sp|\hat{A}(\tau_3)|sp\rangle\rangle = \exp[-i\omega_{sp}\tau_3 - \phi_{sp}\tau_3],$$

the integration by parts over τ_3 as expected from Eq. (8) gives

$$\frac{\exp[-(i\omega_{rp}+\phi_{rp}-i\omega_3)t]}{\hbar(-\omega_{rm}+i\phi_{rm}+\omega_1)}\frac{1}{\hbar(-\omega_{sp}+i\phi_{sp}+\omega_{rp}-i\phi_{rp}-\omega_3)}|s\rangle\langle s|-\vec{\mu}\cdot\tfrac{1}{2}\vec{\epsilon}_3|r\rangle\langle r|\mu_1|m\rangle\rho^{(0)}_{mm}\langle m|\mu_2|p\rangle\langle p|\frac{1}{(-i\hbar)}$$
$$\times\int_{-\infty}^{+\infty}\tfrac{1}{2}\epsilon_1(\xi)e^{-i\omega_1\xi}\tfrac{1}{2}\epsilon_2^*(\xi)e^{i\omega_2\xi}\exp[i\omega_{rp}+\phi_{rp})\xi]d\xi. \quad (15)$$

In general, for any excitation-probe technique with the three basic assumptions stated at the beginning, the density-matrix element providing the polarization between states $|s\rangle$ and $|p\rangle$ is obtained by multiplying the following factors, listed in order of increasing time along the diagram, together. (a) The initial population $\rho^{(0)}_{mm}$. (b) Dipole-matrix element $\langle r|-\mu_1|m\rangle$ associated with the first vertex. (c) Propagator between the first two vertices, in this case,

$$+1/\{\hbar[\omega_1-(\omega_{rm}-i\phi_{rm})]\}.$$

(d) Dipole-matrix element $\langle m|-\mu_2|p\rangle$ associated with the interaction at the second vertex. (e) Effective propagator between the probe and excitation as weighted by the excitation pulse.

$$\pm\frac{1}{i\hbar}\int_{-\infty}^{+\infty}e^{+i\Omega\xi}E_1(\xi)E_2(\xi)\,d\xi,$$

where $E_1(\xi)$ and $E_2(\xi)$ are the electric fields associated with the interactions at vertices (1) and (2), respectively, Ω is the complex resonant frequency of the superposition state of the system at a time before the probing pulse and after the excitation pulses, and the plus (minus) sign is used if the second vertex is on the ket (bra), in this case, $\Omega=\omega_{rp}-i\phi_{rp}$, $E_1(\xi)=\frac{1}{2}\epsilon_1(\xi)e^{-i\omega_1\xi}$, and $E_2(\xi)=\frac{1}{2}\epsilon_2^*(\xi)e^{i\omega_2\xi}$. (f) Coupling factor for the probe vertex $\langle s|-\frac{1}{2}(\vec{\mu}\cdot\vec{\epsilon}_3^*)|r\rangle$. (g) Propagator factor up to time t of the superposition between $|s\rangle$ and $\langle p|$ created by the probe interaction with the

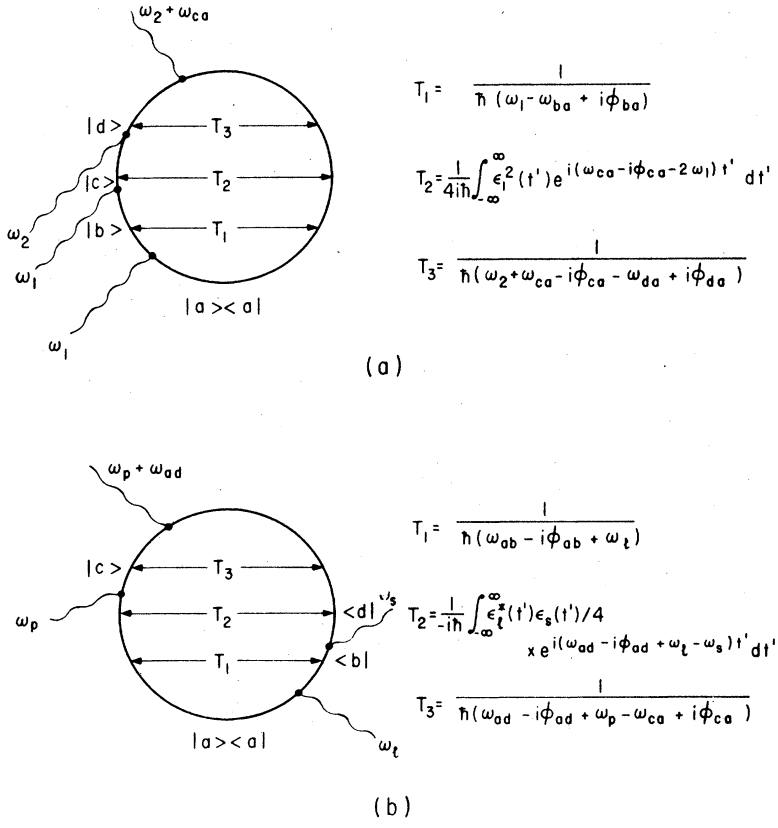

FIG. 8. (a) Diagrammatic representation of a pulsed sum frequency generation process with a two-photon resonance. ω_1 and ω_2 are the two optical carrier frequencies of the temporally nonoverlapped excitation fields. (b) The diagrammatic representation of a pulsed Raman-type process in which $\epsilon_t(t)$ and $\epsilon_s(t)$ are overlapped excitation fields and $\epsilon_p(t)$ a delayed probe field. The system is in a superposition of states $|a\rangle$ and $\langle d|$ after the second interaction.

superposition state after the second interaction vertex as the initial superposition state (in this case, it is between $|r\rangle$ and $\langle p|$). In the present case this propagator is

$$+1/\{\hbar[(-\omega_3+\Omega)-(\omega_{sp}-i\phi_{sp})]\}.$$

(h) The frequency factor $\exp[-i(\Omega-\omega_3)t]$. (i) The ket-bra $|s\rangle\langle p|$ to provide the operator.

The propagator in (g) and the frequency factor can be further clarified by considering a conservation of energy associated with the vertex interactions. Conservation of energy at the first vertex implies that, subsequent to the absorption operation associated with the field containing frequency components around ω_1, the density-matrix element oscillates at $e^{-i\omega_1 t}$. After the second vertex, which is associated with an absorption operation in the neighborhood of frequency ω_2, a net energy absorption equal to $\hbar(\omega_{rp}-i\phi_{rp}-\omega_1+\omega_2)$ has occurred. This is represented by the integral in (e) above which shows it to be extracted from the spectral content of the field product $\epsilon_1\epsilon_2^*$ of the pulses. Thus, after the second vertex and the excitation pulses, a decaying resonant response of the transitions $|r\rangle \rightarrow |p\rangle$ is obtained and thus the density-matrix element has a frequency factor $\exp[-i(\omega_{rp}-i\phi_{rp})t]$. This density-matrix element established between states $|r\rangle$ and $|p\rangle$ is taken into account by adding its energy quanta to the probe-photon energy in the final propagator (g) and in providing the final frequency dependence (h) of the matrix element providing the polarization between states $|s\rangle$ and $|p\rangle$.

With these rules it is possible to analyze many phenomena involving picosecond pulses; the main restricting assumption being that the response is not probed during the excitation.

The pulsed two-photon resonant excitation indicated in Fig. 8(a) in which a third-order density operator has a frequency component at $\omega_2+\omega_{ca}$ which is identical to $\omega_2+2\omega_1$ on exact two-photon resonance is an example. Of more relevance to the present paper is the coherent transient response involving these Raman-type transitions as shown in Fig. 8(b). After the two strong excitation pulses at laser frequency ω_l and Stoke frequency ω_s at the first and the second vertices, respectively, the off-diagonal density operator oscillates at its superposition frequency ω_{ad} and decays with the T_2 response time ($=1/\phi_{ad}$). This is detected by the probe pulse at frequency ω_p. Kaiser, Laubereau, and co-workers[24,25] have performed such experiments for the case in which ω_s is generated through stimulated Raman excitation. In the present case the intermediate states of interest are the rotational states.

VI. COHERENT TRANSIENT ROTATIONAL RAMAN BIREFRINGENCE

We have been particularly concerned with ultrashort-optical-pulse excitations for bandwidths of pulse envelopes which overlap Raman modes, and can thus excite coherent interference through several different Raman mixing processes.[24-28] Probing these excitations to detect polarization can be accomplished either through the observation of radiation scattering off of these excitations[29-32] or by detecting the perturbation in the birefringence of the medium.[28,33] For rotational Raman transitions, the scattered radiation is frequency shifted by a relatively small amount and hence the simpler and superior technique has been the observation of the coherently induced birefringence.

The transient polarization associated with the ground-state rotational Raman spectrum has been considered for linear and symmetric-top molecules for excitation and probe fields of picosecond duration with optical carrier frequencies far removed from any electronic resonances.[26,27] Coherent birefringence bursts associated with this effect for ground electronic-rotational states has been observed in CS_2 vapor at approximately two atmospheres.[28] A similar experiment has been performed for the vibrational Raman transitions of the isotopes of CCl_4.[24]

In the present section, we wish to consider several aspects of the coherent excitation of rotational transient birefringence which are of interest. Of most interest is the resonance enhancement believed possible in Cl_2 in the region of the second harmonic of the 1.06-μm pulses of the glass laser. We also show that there is a possibility of observing excited-electronic-state Raman modes. We wish also to consider decay of the coherent excitations. Picosecond pulses for excitation and probing have been used successfully to study the decay and, in particular, T_2 of vibrational modes in liquids.[25] Similar experiments are possible for rotational transitions in which both the widths of the coherent birefringence peaks and the amplitudes are influenced by populational and polarization decays. We wish finally to establish a relationship between the rotational experiments and similar experiments being performed with typically single-vibrational modes with coherent-anti-Stokes Raman scattering (CARS) techniques.

For these transient Raman effects, there are basically four types of diagrams to consider: the parametric and three time-ordered diagrams with two interaction vertices on each side. The four basic diagrams are those shown in Fig. 9, on which the propagators, states, and fields have

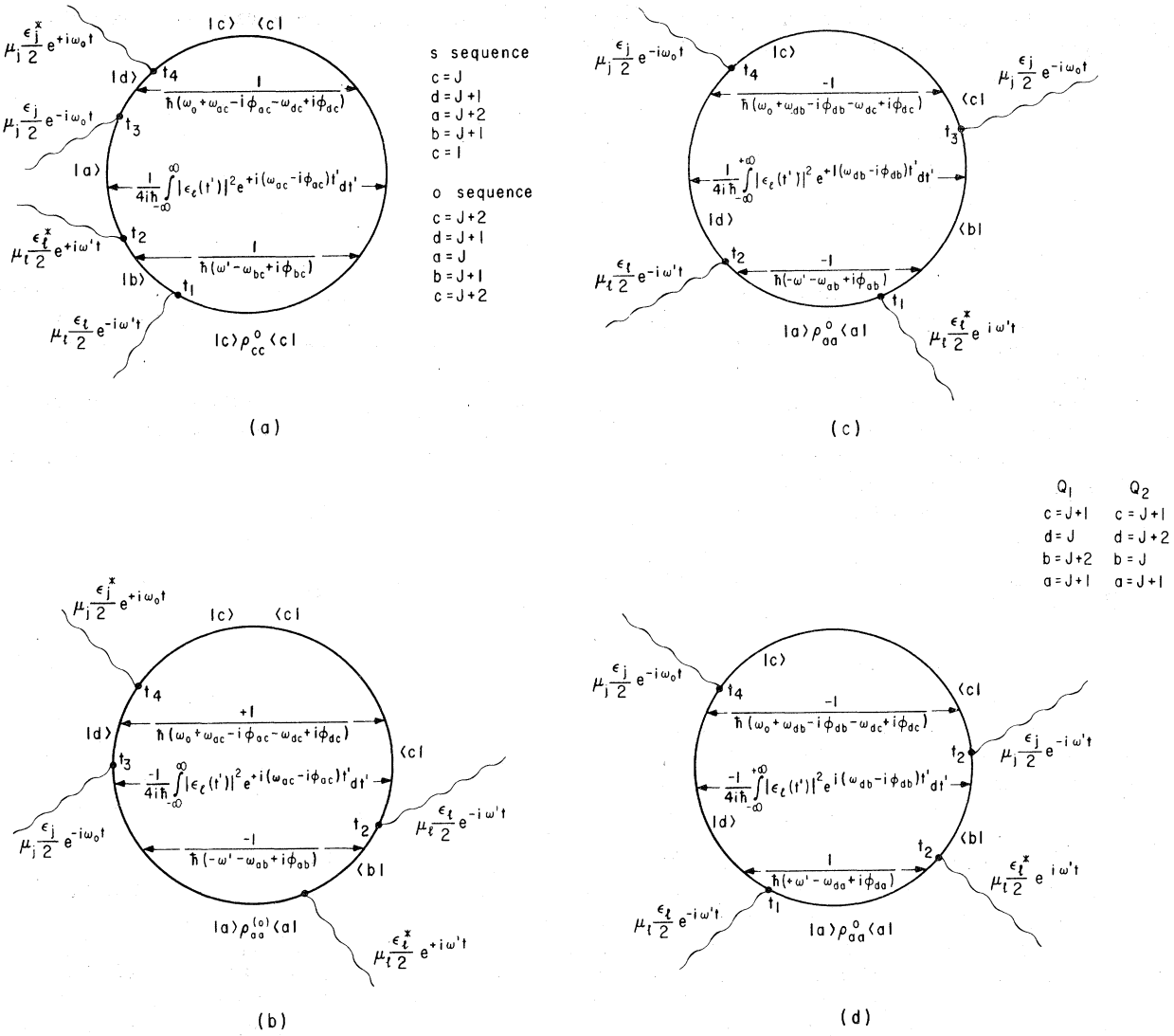

FIG. 9. Four basic diagrams contributing to coherent rotational transient birefringence. (a) The parametric diagram. The two possible sequences of angular momentum values are given. (b) The nonparametric Raman type of diagram contributing Fourier components at the ground-state rotational frequencies. The S and O sequence of J values are also possible for this diagram. (c) and (d) provide Fourier components at the excited-electronic-state rotational frequencies. The two possible sequences of J values, Q_1 and Q_2, are given. For all of these the rules in Sec. V have been used to obtain the propagators. ϵ_l represents the lth component of the excitation-field complex amplitude and ϵ_j that of the probe field amplitude.

been labeled. ϵ_l is assumed to be the laser-field amplitude, μ_l will be taken as the component of $\vec{\mu}$ in the direction of $\vec{\epsilon}_l$. ϵ_j is similarly taken to be the complex amplitude of the field of the probe pulse $\vec{\epsilon}_j$.

State $|a\rangle$, which refers to the initial state (in this case a J, M rotational eigenstate), is assumed to be incoherently populated according to a Boltzmann factor at a temperature T:

$$\rho_{aa}^{(0)} = \frac{\exp[-J(J+1)hBc/kT]}{\sum_{J=\mathrm{Q}}^{\infty}(2J+1)\exp[-J(J+1)hBc/kT]} . \tag{16}$$

For the particular process of interest, the interactions at t_1 and t_2 arise from the same strong optical pulse. The interaction at t_3 is due to a weak probe pulse physically delayed in time from t_2 and t_1. We now evaluate from the rules deduced above

the contributions due to each diagram. For Fig. 9(a), which is the parametric diagram, it is seen that (a)–(h) give for this contribution to the density operator

$$\rho_1^{(3)}(t,t) = -\sum_{a,b,c,d} \frac{|d\rangle\langle d|\tfrac{1}{2}(\vec{\mu}\cdot\vec{\epsilon}_j)|a\rangle \int_{-\infty}^{+\infty} (|\epsilon_1(t')|^2/4i\hbar)\exp[+i(\omega_{ac}-i\phi_{ac})t']dt'}{\hbar(\omega_0+\omega_{ac}-i\phi_{ac}-\omega_{dc}+i\phi_{dc})} \frac{\langle a|\mu_1|b\rangle\langle b|\mu_1|c\rangle}{\hbar(\omega'-\omega_{bc}+i\phi_{bc})}$$

$$\times \rho_{cc}^{(0)}\langle c|\exp[-i(\omega_{ac}-i\phi_{ac}+\omega_0)t]. \tag{17a}$$

In this expression, it is assumed that $\epsilon_1(t)$ is zero for times t such that $\epsilon_j(t)$ is significant. The sum over a,b,c,d is a sum over intermediate, initial, and final states and in this particular case these are sums over the angular momenta J,M at each level subject to the selection rules. These sums will be carried out subsequently.

$\rho_1^{(3)}$ cannot in this case be identified totally with CARS processes although to have a dipole moment the initial state must be the same as the final state. Nonetheless the first process, that associated with the excitation pulse, can be a Raman anti-Stokes process as well as a Stokes process in which case the probing involves coherent Stokes generation.

One obtains for the density-matrix operator attributable to the diagram of Fig. 9(b)

$$\rho_2^{(3)}(t,t) = \frac{-|d\rangle\langle d|\tfrac{1}{2}(\vec{\mu}\cdot\vec{\epsilon}_j)|a\rangle \int_{-\infty}^{\infty} (|\epsilon_1(t')|^2/-4i\hbar)\exp[+i(\omega_{ac}-i\phi_{ac})t']dt'}{\hbar(\omega_0+\omega_{ac}-i\phi_{ac}-\omega_{dc}+i\phi_{dc})} \frac{\rho_{aa}^{(0)}\langle a|\mu_1|b\rangle\langle b|\mu_1|c\rangle\langle c|}{\hbar(\omega'+\omega_{ab}-i\phi_{ab})}$$

$$\times\exp[-i(\omega_{ac}-i\phi_{ac}+\omega_0)t]. \tag{17b}$$

The terms in this expression in general provide Raman-like contributions to the susceptibility since the final state is different from the initial state. Both Stokes and anti-Stokes rotational processes can occur.

The state notation in diagram Fig. 9(b), in particular having $|a\rangle$ as the initial state rather than $|c\rangle$, has been such that the corresponding $\rho_1^{(3)}$ and $\rho_2^{(3)}$ both have frequency components at ω_{ac} which is a ground-electronic-state rotational frequency.

These two diagrammatic contributions to $\rho^{(3)}$ thus provide coherent birefringence associated with the ground-state rotational constant and, furthermore, are the primary contributions when the optical frequencies of the pulses are far removed from any electronic resonance. This can easily be seen from the four diagrams. Only Figs. 9(a) and 9(b) have an emission operation directly following the initial absorption, thereby putting the molecule into a superposition state involving a rotational transition. All that is necessary for a strong rotational excitation is for the amplitude spectrum of the pulse to overlap the rotational transitions. Figures 4(b) and 4(c), on the other hand, involve two initial absorptions bringing the molecule into virtual electronic states. Unless the electronic frequencies are close to resonance, a strong rotational excitation due to the amplitude spectral spread cannot occur. It is also apparent that if such electronic resonances occur, these two diagrams provide susceptibility contributions which involve excited-state frequencies ω_{db}. These excited-state diagrams, evaluated as given by the propagators of Figs. 9(c) and 9(d), provide the following two contributions to the third-order density-matrix elements, respectively:

$$\rho_3^{(3)}(t,t) = \frac{|d\rangle\langle d|\mu_1|a\rangle\rho_{aa}^{(0)}\langle a|\mu_1|b\rangle\int_{-\infty}^{+\infty}(|\epsilon_1(t')|^2/4i\hbar)\exp[i(\omega_{db}-i\phi_{db})t']dt'}{\hbar(+\omega'+\omega_{ab}-i\phi_{ab})}$$

$$\times \frac{\langle b|\tfrac{1}{2}\mu_j\epsilon_j|c\rangle\langle c|}{\hbar(\omega_0+\omega_{db}-i\phi_{db}-\omega_{dc}+i\phi_{dc})}\exp[-i(\omega_{db}-i\phi_{db}+\omega_0)t], \tag{18a}$$

and

$$\rho_4^{(3)}(t,t) = \frac{|d\rangle\langle d|\mu_1|a\rangle\rho_{aa}^{(0)}\langle a|\mu_1|b\rangle\int_{-\infty}^{+\infty}(|\epsilon_1(t')|^2/-4i\hbar)\exp[i(\omega_{db}-i\phi_{db})t']dt'}{\hbar(\omega'-\omega_{da}+i\phi_{da})}$$

$$\times \frac{\langle b|\tfrac{1}{2}\mu_j\epsilon_j|c\rangle\langle c|}{\hbar(\omega_0+\omega_{db}-i\phi_{db}-\omega_{dc}+i\phi_{dc})}\exp[-i(\omega_{db}-i\phi_{db}+\omega_0)t]. \tag{18b}$$

For these diagrams to have ω_{db} nonzero, one observes that one side of the diagram must involve a Stokes process and the other side an anti-Stokes process. This, in turn, demands that the final state be the same as the initial state.

VII. ROTATIONAL COHERENT TRANSIENT BIREFRINGENCE RESONANTLY ENHANCED

The expressions for the transient evolution of the dipole moment as given by Eqs. (17) and (18) will now be considered in more detail for exciting intensity profiles possessing spectral spreads sufficient to overlap rotational transitions. When, in addition to this spectral spread, the frequencies of the incident radiation fields are sufficiently close to single-photon resonances, considerable enhancement of the polarization is possible and is expected experimentally to provide a sensitive time-resolved spectroscopy.

We treat here the response of a linear molecule with its $2J+1$ degenerate rotational eigenstates $|a\rangle = |JM\rangle$. The $\hat{A}(\tau)$ operators are not strictly diagonal in the sense of Eq. (6a) with $a = |J_a, M_a\rangle$ and $b = |J_b, M_b\rangle$, since M_a and M_b change during a collision. Although rotational invariance allows one to form coupled states given by[5,10]

$$|J_a J_b KQ\rangle\!\rangle = \sum_{m_a m_b} (-1)^{j_b - m_b} |j_a m_a, j_b m_b\rangle\!\rangle \times \langle j_a j_b m_a - m_b | KQ\rangle , \tag{19}$$

where $\langle j_a j_b m_a - m_b | KQ\rangle$ is the Clebsch-Gordan vector-coupling coefficient, for which $\hat{A}$ is diagonal in K and Q, the evaluation of the matrix elements is difficult, and which is diagonal in j_a and j_b only for isolated lines for the various intermultiplet transitions. γ_{ab}^{c} is then a function of K and provides the relaxation rate of the K multipole between levels a and b. For present calculations, we neglect this multipole behavior and calculate the density-matrix contributions of Eqs. (17) and (18) assuming that the matrix elements are independent of M_a and M_b and that the most important matrix elements of $\hat{A}$ are the diagonal terms. This provides the same effective decay rate for each of the degenerate rotational superposition states prepared by the initial optical pulse (the region of the diagrams having the effective propagator involving the integral of the squared amplitude of the optical pulse). Thus we use the rotational eigenstates $|J_a, M_a\rangle$ directly for a numerical estimate of the polarizations due to Eqs. (17) and (18). As pointed out by Omont, the more accurate approach considering the individual multipole contribution provides an analogous result except for a weighted sum over the individual multipole decay rates.[5]

Using the more compact notation $(\mu_j)_{bc} = \langle b | \mu_j | c\rangle$, we now wish to combine the polarization terms resulting from Eqs. (17a) and (17b) and Eqs. (18a) and (18b). The combined Eq. (17), as previously discussed, is expected to be the dominant off-resonance contribution; Eqs. (18), the electronically resonant contributions involving the excited-state rotational constant.

If $\vec{\epsilon}_1(t')$, the electric field of the exciting pulse, is assumed polarized in z direction, then the macroscopic dipole moment $\vec{P}_1$ due to the processes shown in Figs. 9(a) and 9(b) (using $\omega_{ac} - \omega_{dc} = \omega_{ad} = -\omega_{da}$), is given by

$$\vec{p}_1 = -\sum_{J_a, J_b, J_c, J_d} \frac{1}{2} \sum_M [(\vec{\mu}_{cd})(\vec{\mu}_{da} \cdot \vec{\epsilon}_j)(\mu_z)_{ab}(\mu_z)_{bc}] \times \int_{-\infty}^{\infty} \left(\frac{|\epsilon_1(t')|^2}{4i\hbar}\right) \exp[i(\omega_{ac} - i\phi_{ac})t'] \, dt' \left(\frac{1}{\hbar(\omega_0 - \omega_{da} - i(\phi_{ac} - \phi_{dc})}\right) \times \left[\frac{\rho_{cc}^{(0)}}{\hbar(\omega' - \omega_{bc} + i\phi_{bc})} - \frac{\rho_{aa}^{(0)}}{\hbar(\omega' - \omega_{ba} - i\phi_{ab})}\right] \exp[-i(\omega_{ac} - i\phi_{ac} + \omega_0)t] . \tag{20}$$

Similarly the two excited-state contributions, when combined, give a polarization contribution $\vec{p}_2$:

$$\vec{p}_2 = \sum_{J_a, J_b, J_c, J_d} \frac{1}{2} \sum_M [\vec{\mu}_{cd}(\mu_z)_{da}(\mu_z)_{ab}(\vec{\mu} \cdot \vec{\epsilon}_j)_{bc}] \times \int_{-\infty}^{+\infty} \left(\frac{|\epsilon_1(t')|^2}{4i\hbar}\right) \exp[i(\omega_{db} - i\phi_{db})t'] \, dt' \times \rho_{aa}^{(0)} \left[\left(\frac{1}{\hbar(\omega_0 + \omega_{cb} - i(\phi_{db} - \phi_{dc})}\right)\left(\frac{1}{\hbar(\omega' - \omega_{ba} - i\phi_{ab})} - \frac{1}{\hbar(\omega' - \omega_{da} + i\phi_{da})}\right)\right] \times \exp[-i(\omega_{db} - i\phi_{db} + \omega_0)t] . \tag{21}$$

To proceed, it is necessary to consider the Raman Stokes and anti-Stokes contributions to the sums over J_a, J_b, J_c, and J_d and the sum over the magnetic quantum number M. We neglect the transitions which make a and c the same in Eq. (20) (Q-branch Raman transitions) and b and d in Eq. (21) (S- and O-branch Raman transitions) which contribute a Rayleigh component at the probe frequency. The corresponding terms are zero when loss is neglected since the large square brackets in Eqs. (20) and (21) are then identically zero.

From the dipole selection rules for linear polarization, which we consider here, $\Delta J = \pm 1$, $\Delta M = 0$, there are only two nonzero sequences in the sums over the angular momentum quantum numbers. For Figs. 9(a) and 9(b), we choose to write these as $J_a = J$, $J_b = J+1$, $J_c = J+2$, $J_d = J+1$, and $J_a = J+2$, $J_b = J+1$, $J_c = J$, $J_d = J+1$, respectively. The second is the anti-Stokes sequence in accordance with nomenclature from CARS for Fig. 9(b) and the first is the Stokes sequence for diagram 9(b). For diagram 9(a) it is the reverse, the second sequence being that of the Stokes and the first that of the anti-Stokes sequence. We shall refer to these in accordance with the Raman notation for Fig. 9(b); the first sequence thus being the O sequence and the second the S sequence.

For the diagrams of Figs. 9(c) and 9(d) [as described by Eq. (21)], the excited-state contribution arises from the interference between the two possible Q-branch Raman contributions. The two possible selections of the J's shown ($J_a = J+1$, $J_b = J+2$, $J_d = J$, $J_c = J+1$, and $J_a = J+1$, $J_b = J$, $J_d = J+2$, $J_c = J+1$) correspond to an interchange of the Stokes and anti-Stokes sequence on the two sides. Taking the Raman notation, we shall refer to these as the Q_1 and Q_2 sequences for these two diagrams.

The periodic nature of the polarization arises from the final sum over all possible values of J for these four sequences (S, O, Q_1, and Q_2). The significant values of J which must be included are determined by the initial populations $\rho_{aa}^{(0)}$ [Eq. (16) for a Boltzmann distribution] and the spectrum of the pulse amplitude which provides the strength of the Fourier components at the rotational Raman frequencies. Since these are evenly spaced, $\omega_{J+2,J} = 4\pi Bc(2J+3)$ with $J = 0, 1, \ldots$ and B the rotational constant [excited state for (21) and ground state for Eq. (20)], the basic period being $1/(2Bc)$, periodic bursts in the polarization induced by the probe pulse are observed. Bursts are also observed halfway between the fundamental period, these bursts having a time-reversed amplitude profile with respect to those at the fundamental period. In addition nuclear spin can introduce additional bursts. For CS_2, J odd is not possible for the rotational frequencies above which is introduced a burst at $1/8Bc$ following the excitation pulse.[28]

With Eqs. (20) and (21) we can consider the frequency behavior and time evolution (damping and widths) of the periodic birefringence bursts associated with the ground state and the electronic excited state. The damping in the first approximation (all ϕ_{db} equal) provides an exponential decay of the coherence without any influence upon the temporal profiles. Experimentally, investigations of the width of the coherent bursts and their temporal decay will be interesting with regard to both this approximation and the initial neglect of the product state formalism to evaluate the matrix elements for $\hat{A}$.

The frequency dependence of the two contributions Eqs. (20) and (21) are quite different. Far below resonance we can set $\omega_{bc} \simeq \omega_{ba} \simeq \omega_{da} \equiv \omega_e$, the electronic-transition frequency, this being accurate to within the rotational frequency. Neglecting linewidth, Eq. (20) indicates that $\vec{p}_1$ is then $\sim[1/(\omega_e)^2](\rho_{cc}^{(0)} - \rho_{aa}^{(0)})$ and is generally appreciably larger than $\vec{p}_2 \sim \rho_{aa}^{(0)}[1/(\omega_e)^2](\omega_{db}/\omega_e)$ from Eq. (21). ω_{db} is ideally a rotational transition frequency $\simeq 10^{11}$ rad/sec. Thus, the ratio p_2/p_1 has a maximum value of

$$\sim \frac{10^{11}}{10^{15}}\left(\frac{\rho_{aa}^{(0)}}{\rho_{cc}^{(0)} - \rho_{aa}^{(0)}}\right) \sim 10^{-2}$$

for typical molecules (CS_2 at 296 °C). This is most likely an overestimate since only a single electronic transition has been assumed.

Thus, we conclude that the dominant coherent rotational response below resonance comes from the Stokes and anti-Stokes sequences of Eq. (20) and hence the first two diagrammatic contributions of Fig. 9. In this limit, Eq. (20) reduces to the previously calculated index-of-refraction change for the coherent response.[27] This can be shown by considering Eq. (20) for the probe field $\vec{\epsilon}_j$ polarized in the z direction. We express the sum over M of the matrix elements which enter into the induced polarization [Eq. (20)] in the z direction in terms of the matrix elements $\mu_{\parallel}$, the purely electronic dipole moment parallel to the linear molecular axis, and $\mu_{\perp}$, that which is perpendicular to the linear molecular axis between the two electronic states. For either the Stokes or anti-Stokes sequence, one obtains[34]

$$\sum_M (\mu_z)_{cd}(\mu_z)_{da}(\mu_z)_{ab}(\mu_z)_{bc} = \sum_M |(\mu_z)_{ca}|^2 |(\mu_z)_{ac}|^2 = \frac{2(J+1)(J+2)}{15(2J+3)}(|\mu_{\parallel}|^2 - |\mu_{\perp}|^2)^2. \quad (22)$$

Introducing the electronic polarizability parallel to the molecular axis $\alpha_{\parallel}(\omega) = |\mu_{\parallel}|^2/[\hbar(\omega - \omega_e)]$ and that perpendicular to the molecular axis $\alpha_{\perp}(\omega) = |\mu_{\perp}|^2/[\hbar(\omega - \omega_e)]$, we see that Eq. (20), when damping is neglected and for the 0 sequence, can be approximately written

$$(p_1)_z \simeq -\sum_J \exp[-i(\omega_{J,J+2})t](\rho_{J+2,J+2} - \rho_{JJ}) \times \Delta\alpha(\omega')\Delta\alpha(\omega_0)\frac{2}{15}\frac{(J+1)(J+2)}{(2J+3)} \times \int_{-\infty}^{+\infty} \frac{|\epsilon_I(t')|^2}{4i\hbar} \exp[+i(\omega_{J,J+2})t'] \times dt' \tfrac{1}{2}\epsilon_z e^{-i\omega_0 t}. \quad (23)$$

$\omega_{J,J+2}$ is the rotational transition frequency of the $J \to J+2$ transition $\omega_J - \omega_{J+2} = -4\pi Bc(2J+3)$ and $\Delta\alpha(\omega) = \alpha_{\parallel}(\omega) - \alpha_{\perp}(\omega)$. The S sequence gives the complex conjugate of the complex susceptibility index of Eq. (23) $[\Delta\chi_1 \equiv 2(p_1)_z/\epsilon_z e^{-i\omega_0 t}]$ and thus the total susceptibility is $2\,\mathrm{Re}(\Delta\chi_1) = 2\Delta\chi_1''$ which is identical to that previously obtained using the classical effective Hamiltonian[27]

$$H' = -\tfrac{1}{4}[\tfrac{1}{2}\Delta\alpha(\omega)\sin^2\theta - \alpha_{\perp}(\omega)]\,|E_0(t)|^2. \quad (24)$$

Similarly, Eq. (21) can, with the same approximations, be writtten for the Q_1 sequence

$$(p_2)_z = \sum_J \exp[-i(\omega^e_{J,J+2})t]\rho^{(0)}_{J+1,J+1}\Delta\alpha(\omega_0)\Delta\alpha(\omega')\frac{2}{15}\frac{(J+1)(J+2)}{(2J+3)} \times \int_{-\infty}^{+\infty} \frac{|\epsilon_I(t')|^2}{4i\hbar} \exp[i\omega^e_{J,J+2}t']\,dt'\left[\frac{\omega^e_{J+2,J}}{\omega' - \omega_e}\right]\frac{\epsilon_z e^{-i\omega_0 t}}{2} = \Delta\chi_2(\omega_0)\tfrac{1}{2}\epsilon_z e^{-i\omega_0 t}, \quad (25)$$

where $\omega^e_{J,J+2} = \omega_{db}$, the rotational transition frequency in the excited state, $= -4\pi B_e c(2J+3)$. B_e is the excited-state rotational constant. As above, the Q_2 sequence gives the complex-conjugate susceptibility $\Delta\chi_2(\omega)^*$ so that the total susceptibility is $2\,\mathrm{Re}(\Delta\chi_2) = 2\Delta\chi_2''$.

Equations (20) and (21) show that considerable resonance enhancement of the coherent rotational response can be obtained from the electronic resonances. In particular $\vec{p}_2$, the excited-state contribution, can become of the same order of magnitude as $\vec{p}_1$ or larger since $(\omega_{da} - \omega_{ba})/(\omega' - \omega_{da} + i\phi_{da})$, coming from the square bracket in Eq. (21), can probably be made to exceed $(\rho^{(0)}_{cc} - \rho^{(0)}_{aa})/\rho^{(0)}_{aa}$ by an order of magnitude or so.

Theoretically, since the matrix elements are in general not known, it is difficult to calculate the refractive-index change from Eqs. (20) and (21). Based on Eqs. (23) and (25), we have estimated the values of $2\Delta\chi_1''$ and $2\Delta\chi_2''$ as a function of frequency from the known susceptibility for O_2. With subpicosecond pulse excitation at room temperature approximately 15 rotational states provide significant contributions. The calculated results are shown in Figs. 10 and 11. Both $\Delta\chi_1''$ and $\Delta\chi_2''$ exhibit the resonances associated with the linear susceptibility. $\Delta\chi_2''$ has an additional resonant enhancement due to the additional term $1/(\omega' - \omega_e)$ in Eq. (25). For O_2,[35] it is estimated that $\Delta\chi_2''$ becomes larger than $\Delta\chi_1''$, although the approximations limit the validity of $\Delta\chi_1''$ and $\Delta\chi_2''$ given by Eqs. (23) and (25) in the region $|\omega' - \omega_e|$

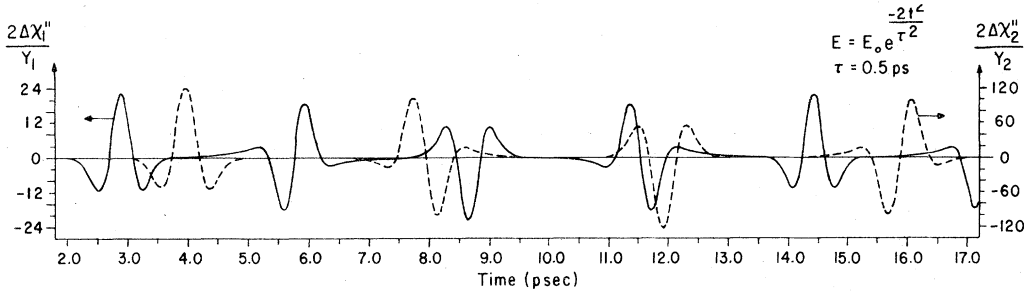

FIG. 10. Theoretically predicted susceptibility change induced by a Gaussian optical-laser pulse in O_2 at room temperature. The solid curve has a fundamental period $(2B_0c)^{-1}$ and a subperiod $(4B_0c)^{-1}$, and arises from the diagrams of Figs. 9(a) and 9(b). The dashed curve has a fundamental period $(2B_1c)^{-1}$ and a subperiod $(4B_1c)^{-1}$ and arises from the excited-state diagrams of Figs. 9(c) and 9(d). Y_1 and Y_2 are two constants specified in Fig. 11. For O_2, $B_0 = 1.446\ \mathrm{cm}^{-1}$ and $B_1 = 1.05\ \mathrm{cm}^{-1}$ (Ref. 35). Here, the effect of the nuclear-spin statistics which demand the absence of odd J has also been taken into account (Ref. 28).

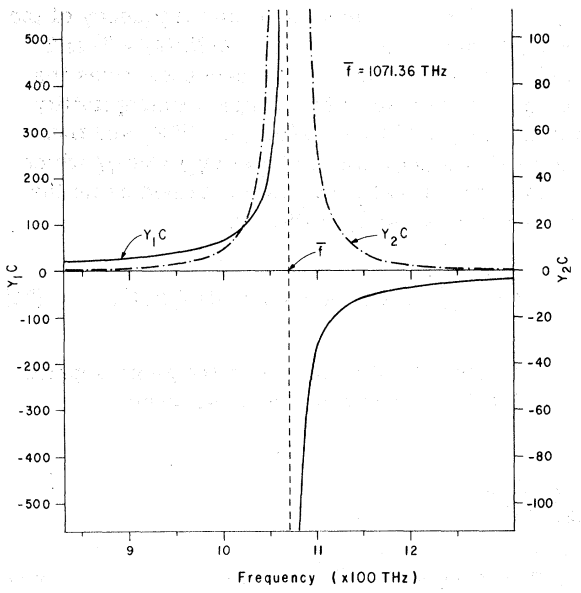

FIG. 11. Resonant enhancement of $\Delta\chi_1''$ and $\Delta\chi_2''$. The electronic transition is $^3\Sigma_g^- \rightarrow {}^3\Sigma_u^+$. The solid curve corresponds to $\Delta\alpha(\omega')$ and the dash-dotted curve corresponds to $\Delta\alpha(\omega')/(\omega'^2-\omega_\theta^2)$, $C=15\ \hbar\chi_0\times10^{41}/2\Delta\alpha(\omega_0)NE_0^2$ in cgs units, $\Delta\alpha(\lambda=5893\ \text{Å})=11.4\times10^{-25}$ esu (Ref. 35) and χ_0, the linear susceptibility.

$\leq 4\pi/\tau$, where τ is the pulse width.

Experimentally, it appears possible to observe a resonant enhancement of coherent transient birefringence in Cl_2 at the second harmonic of the Nd^{3+} laser. Verification of the excited-state contribution is also possible and is presently being pursued.

In the present section, we have considered exclusively coherent rotational effects associated with a ground state and an excited electronic state. If two phase-related coherent pulses with complex amplitudes $\epsilon_1 e^{-i\omega_1 t}$ and $\epsilon_2 e^{-i\omega_2 t}$, with frequencies ω_1 and ω_2 differing by a vibrational resonant frequency, are used to excite the medium, one field at t_1 and the other at t_2 of the diagrams of Fig. 9 or t_1 and t_1' in Fig. 1, then the molecule is thrown into a rotational sublevel of the vibrational state by the excitation. Thus, in conventional CARS, an exact-vibrational-resonance coherent transient rotational birefringence should be observable. The probe pulse in this case would correspond to vibrational anti-Stokes scattering. As $\omega_1-\omega_2$ is tuned off of the vibrational resonance the integral in Eq. (14b) can be approximately integrated as

$$\frac{\exp\{+[i\omega_{rp}-i(\omega_1-\omega_2)+\phi_{rp}](t-\tau_3-\cdots)\}}{+[i\omega_{rp}-i(\omega_1-\omega_2)+\phi_{rp}]}\epsilon_1\epsilon_2^*,$$

and the susceptibility goes over to the monochromatic CARS susceptibility. Thus the rotational coherent response would be expected to disappear with detuning. This coherent rotational effect for properly shaped picosecond pulses can be large and might provide a means of observing CARS without the bothersome interference associated with nonvibrationally resonance terms contributing a nonresonant susceptibility in monochromatic CARS experiments.

VIII. CONCLUSIONS

In the present paper we have investigated the diagrammatic representation of density-matrix elements. In general, a diagram is used to represent two sequences of interactions, one of which is associated with the wave function and which is time ordered with respect to the second interaction sequence which is associated with the complex conjugate of the wave function. Each of the two sequences represents a possible time evolution of the molecular state. The time-ordered diagram portrays the interference between the two possible evolutions which gives rise to dipole moments and population changes. Each diagram corresponds to one term of the density matrix and a set of rules can be used to deduce polarization directly from them for monochromatic interactions and many pulsed interactions. In the absence of broadening, it has been shown that the sum of all possible time-ordered graphs for a particular set of interactions on the wave function and a particular set on the complex-conjugate wave function results in a term which is independent of the time ordering of the wave function interactions with respect to those of the complex-conjugate wave function. It is easily established that the conditions for this to be true can be relaxed to $\phi_{nn}=0$ if n is the initial state and $\phi_{n'n}+\phi_{nn''}=\phi_{n'n''}$ for any other states n' and n''. This is also called the damping approximation. The evolution of the density operator can then be determined by the product of the evolution of the wave function and that of its complex conjugate taken separately. Calculations of nonlinear polarizations from the resultant non-time-ordered graphs are well known and are described in the literature.

The time-ordered propagator approach uniquely identifies a particular perturbation process; in many cases it allows a simplification of the calculations by employing the general rules; and it should provide a means of conveniently incorporating broadening processes more rigorously. In the present paper, we have considered several processes including second-harmonic generation, coherent anti-Stokes Raman scattering, and coherent transient birefringence. The combination

of time-ordered terms in the damping approximation was illustrated with the diagrams for the Raman effect. Resonant denominators for which the transition frequencies are solely between the initial state and excited states result, as is evident from Fig. 5.

Transient perturbations when viewed diagrammatically can in many cases be interpreted clearly. For the Raman effect, it has recently been shown that the time-ordered diagram of Fig. 4(a) provides the transient Raman response, and Figs. 4(b) and 4(c) the hot luminescence (HL) transients as defined by Shen.[21] As is apparent from the diagrams, the HL terms involve the density-matrix element $\rho_{n'n}$ propagated by T_2. With n' usually equal to n, this is equivalent to the decay of the excited-state population. In the present paper, we have deduced calculational rules for a special class of transient interactions for which the system is on resonance after the second interaction vertex (Fig. 1) and this excitation is probed by a delayed pulse. Several new aspects of rotational coherent transient birefringence are treated. When the excitation frequency is far removed from a single-photon resonance, only two time-ordered diagrams [Figs. 9(a) and 9(b)] have been shown to contribute to the susceptibility, and coherent bursts in the birefringence separated by $(4B_0c)^{-1}$ are obtained, where B_0 is the rotational constant of the ground rotational states. As the excitation frequency approaches a single-photon resonance, two additional diagrams [Figs. 9(c) and 9(d)] become important and contribute terms which result in coherent bursts separated by $(4B_1c)^{-1}$, where B_1 is the rotational constant of the excited state involved in the first-vertex interaction. Apart from the rotational coherent transient birefringence, the rules deduced can be used to obtain the pulsed responses of CARS experiments and coherent pulsed two-photon excitation.

The diagrammatic approaches can also be used to evaluate transition probabilities since

$$\frac{\partial \rho_{cc}}{\partial t} = \sum_a \frac{i}{\hbar}(\rho_{ca}H_{ac} - H_{ca}\rho_{ac}).$$

The polarization terms ρ_{ac} are evaluated up to the order desired. Taking twice the imaginary part of ρ_{ac} multiplied by $H_{ca}/\hbar$ then immediately provides the transition rate. This reduces to the usual Fermi "golden rule" when both sides of the density-matrix diagram are the same in terms of interactions and states involved.

The density-matrix diagrams can easily be generalized to include other types of interactions. Photon exchange between different molecular species through the introduction of the photon propagator and the treatment of tunneling phenomena by the transfer Hamiltonian are two such interactions which have been considered.

ACKNOWLEDGMENTS

This research was supported in part by the Army Research Office under Grant No. DAHCO4-75-C 0095, the National Aeronautics and Space Administration under Grant No. NSG-2151, and the National Science Foundation under Grant No. ENG72-03960-A01.

[1]N. Bloembergen, *Nonlinear Optics* (Benjamin, New York, 1965).
[2]J. F. Ward, Rev. Mod. Phys. 37, 1 (1965).
[3]D. Marcuse, *Engineering Quantum Electrodynamics* (Harcourt Brace Jovanovitch, New York, 1970).
[4]A. M. Bonch-Bruevich and Y. A. Khodovoi, Usp. Fiz. Nauk. 85, 3 (1965) [Sov. Phys. Usp. 8, 1 (1965)].
[5]A. Omont, E. W. Smith, and J. Cooper, Astrophys. J. 175, 185 (1972).
[6]M. C. Bordé, C. R. Acad. Sci. (Paris) 282B, 341 (1976).
[7]T. K. Yee, T. K. Gustafson, S. A. J. Druet, and J.-P. E. Taran, Opt. Commun. 23, 1 (1977).
[8]C. P. Slichter, *Principles of Magnetic Resonance* (Harper and Row, New York, 1963), p. 134.
[9]J. D. Bjorken and S. D. Drell, *Relativistic Quantum Mechanics* (McGraw-Hill, New York, 1964), p. 77.
[10]Michel Baranger, Phys. Rev. 111, 494 (1958); 111, 481 (1958).
[11]L. I. Schiff, *Quantum Mechanics* (McGraw-Hill, New York, 1968).
[12]P. N. Butcher, *Non-linear Optical Phenomena* (Engineering Experiment Station, Ohio State University, Columbus, 1965).
[13]Energies are taken as $-\hbar\omega$ on the bra side, where ω is the positive frequency of the photon field. This agrees with the convention adopted in Fig. 2.
[14]P. D. Maker and R. W. Terhune, Phys. Rev. A 137, 801 (1965).
[15]M. D. Levenson and N. Bloembergen, Phys. Rev. B 10, 4447 (1974).
[16]P. R. Regmer and J. P. E. Taran, Appl. Phys. Lett. 23, 240 (1973).
[17]R. F. Begley, A. B. Harvey, and R. K. Byer, Appl. Phys. Lett. 25, 387 (1974).
[18]Won B. Roh, Paul W. Schreiber, and J. P. E. Taran, Appl. Phys. Lett. 29, 174 (1976).
[19]See Francois Moya, Ph.D. thesis (l'Université de Paris-Sud, 1976) (unpublished); see also Technical Report No. 1975–13, Office Nationale d'Études et Récherches Aerospatiales.
[20]Resonant cw and transient CARS is considered in detail by S. Druet, B. Attal, J.-P. E. Taran, and T. K. Gustafson (unpublished).
[21]Y. R. Shen, Phys. Rev. 139, 622 (1974).
[22]A. Messiah, *Quantum Mechanics* (Wiley, New York, 1962), Vol. 2.

[23]Robert T. Lynch, Jr., Haim Lotem, and N. Bloembergen, in Conference on Lasers in Chemistry, Royal Institution, London, 1977 (unpublished).
[24]D. Von der Linde, A. Laubereau, and W. Kaiser, Phys. Rev. Lett. 26, 954 (1971).
[25]A. Laubereau and W. Kaiser, Ann. Rev. Phys. Chem. 26, 83—99 (1975).
[26]C. H. Lin, J. P. Heritage, and T. K. Gustafson, Appl. Phys. Lett., 19, 397 (1971).
[27]C. H. Lin, J. P. Heritage, T. K. Gustafson, R. Y. Chiao, and J. P. McTague, Phys. Rev. A13, 813 (1976).
[28]J. P. Heritage, T. K. Gustafson, and C. H. Lin, Phys. Rev. Lett. 34, 1299 (1975).
[29]R. L. Shoemaker and R. G. Brewer, Phys. Rev. Lett. 28, 1430 (1972).
[30]R. G. Brewer and E. K. Hahn, Phys. Rev. A 8, 464 (1973).
[31]S. Haroche, J. A. Parsner, and A. L. Schawlow, Phys. Rev. Lett. 30, 948 (1973).
[32]S. Haroche, M. Gross, and M. P. Silverman, Phys. Rev. Lett. 33, 1063 (1974).
[33]D. Heiman, R. W. Hellwarth, M. D. Levenson, and Graham Martin, Phys. Rev. Lett. 36, 189 (1976).
[34]C. H. Townes and A. K. Schawlow, *Microwave Spectroscopy* (Dover, New York, 1975), Chap. 1.
[35]For the data of $\Delta\alpha(\omega)$, see J. Applequist, J. R. Carl, and K. K. Fung, J. Am. Chem. Soc. 94, 2952 (1972). For the data of rotational constants, see G. Herzberg, *Spectra of Diatomic Molecules*, 2nd ed. (Van Nostrand Reinhold, New York, 1950), pp. 66–73.